3rd of 5 files

Chapter 5

EFFECT OF STRESS ON INITIATION AND PROPAGATION OF LOCALIZED CORROSION IN ALUMINIUM ALLOYS

By

SUKANTA GHOSH

A thesis submitted to
University of Birmingham
for the degree of
DOCTOR OF PHILOSOPHY
Metallurgy and Materials
School of Engineering
University of Birmingham

November 2007

5 MICRO-CAPILLARY ELECTROCHEMICAL CELL STUDIES OF THE CORROSION BEHAVIOUR OF INTERMETALLIC PARTICLES IN AA2024-T351

The electrochemical behaviour of the two predominant types of intermetallic particles (Fe-Mn particle and ‘S’ phase particle)[16] in AA2024-T351 was studied using the micro-capillary electrochemical cell technique. Normally pitting in aluminium alloys is associated with the intermetallic/constituent particles. However the mechanism of pit initiation is not fully understood yet. The role of different intermetallic particles on corrosion of aluminium alloys has been investigated by different researchers in last few decades [8-11, 14, 37, 38, 40, 42, 47, 48, 82, 123, 171, 173, 175, 181-197]. Among the several techniques used to investigate the reactivity of intermetallic particles, microcapillary electrochemical cell technique is the most attractive one [39-42]. Small diameter of the micro capillaries allows electrochemical tests to be performed on selective particles/areas without exposing the whole surface. Thus, the microcapillary electrochemical cell technique provides the opportunity to compare the relative electrochemical activity of the site of interests. The main focus of this chapter is to find out the relative corrosion behaviour of different intermetallic particles present in AA2024-T351 along with the behaviour of particle free matrix. This study will provide insight into the contribution of different intermetallic particles towards the initiation of pitting corrosion in AA2024-T351 and thereby determine its localized corrosion behaviour.

---

[16] Compositional and morphological analysis of both types of intermetallic particles has already been discussed in details in Chapter 4.

5.1 Anodic Potentiodynamic Polarization Measurements

Anodic polarization scans were performed on Fe-Mn particles, 'S' phase particles and the particle free matrix of AA2024-T351 in naturally aerated 0.1 M NaCl solution using a capillary of 40 micron diameter. Two different micro-capillary electrochemical cell set ups[17] were used in this current study to confirm the consistency of the findings for each type of experiments. Results obtained from both set up showed similar trend and were found to be consistent with each other. Final polishing of all samples was performed using one micron diamond suspension and after final polishing, samples were kept 1.5 – 2 hours in air before starting the tests.[18]

Figure 5.1 shows the comparisons of the anodic polarization scans on the Fe-Mn particle, 'S' phase particles and matrix starting from -1000 mV vs. Ag/AgCl at a scan rate of 1 mV/s. It should be noted that in all cases potentiodynamic polarization scans were started directly from a specified potential (referred as 'scan start potential') without any initial wait at the open circuit potential. The measured pH of the naturally aerated 0.1 M NaCl solution used in microcapillary electrochemical cell experiments was about ~ 5.6. It can clearly be seen from Figure 5.1 that 'S' phase particles show the lowest pitting potential. Rapid increase in the current occurs as soon as the potentiodynamic scans enter the anodic domain right after the corrosion potential. 'S' phase particles show corrosion potential between -700 mV and -600 mV vs. Ag/AgCl. Cathodic reactivity of both 'S' phase particles and Fe-Mn particles are almost an order of magnitude higher than the

---

[17] One micro-capillary electrochemical cell set up was used in the University of Birmingham, UK and the second set up was at the Université de Bourgogne, Dijon, France. Details of the micro-capillary electrochemical cell set up can be found in Chapter 3.

[18] Details of the sample preparation for micro-capillary electrochemical tests can be found in Chapter 3.

particles free matrix (~200 µA/cm^2 for the particles as opposed to ~20 µA/cm^2 for the matrix). Moreover, with a scan rate of 1 mV/s, Fe-Mn particles show much higher corrosion potential than either 'S' phase particles or the matrix when scanned from -1000 mV vs. Ag/AgCl. Corrosion potentials of the Fe-Mn phases are very consistent and show a value around -400 mV vs. Ag/AgCl. All Fe-Mn particles show a definite passive region between the corrosion potential and breakdown. Breakdown potentials of the Fe-Mn particles are about -200 mV vs. Ag/AgCl. In very few cases current went negative (cathodic) prior to the breakdown (as shown by the firm black line in Figure 5.1) of the Fe-Mn particles. This could be due to the reduction of some species/elements, but the exact reason behind this phenomenon is not fully understood yet. Matrix phase show corrosion potential around -600 mV vs. Ag/AgCl and after a clear passive region it breaks down at ~-400 mV vs. Ag/AgCl.

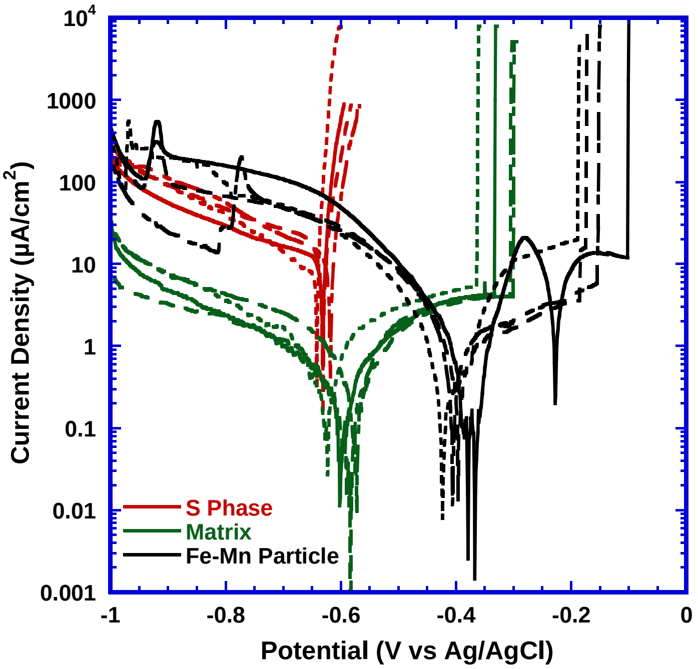

Figure 5.1 Comparison of anodic polarization curves of different phases of AA2024-T351 in naturally aerated 0.1 M NaCl measured using capillary of 40 µm diameter. Scan start potential was -1000 mV vs. Ag/AgCl with a scan rate of 1 mV/s.

Figure 5.2 shows the comparison of the potentiodynamic scans between the Fe-Mn particles and the matrix when scan start potential is -800 mV vs. Ag/AgCl. Potentiodynamic scans of Figure 5.2 were performed in a similar manner as shown in Figure 5.1 except the fact that scan start potential for scans in Figure 5.2 was -800 mV vs. Ag/AgCl as opposed to -1000 mV vs. Ag/AgCl discussed in Figure 5.1.

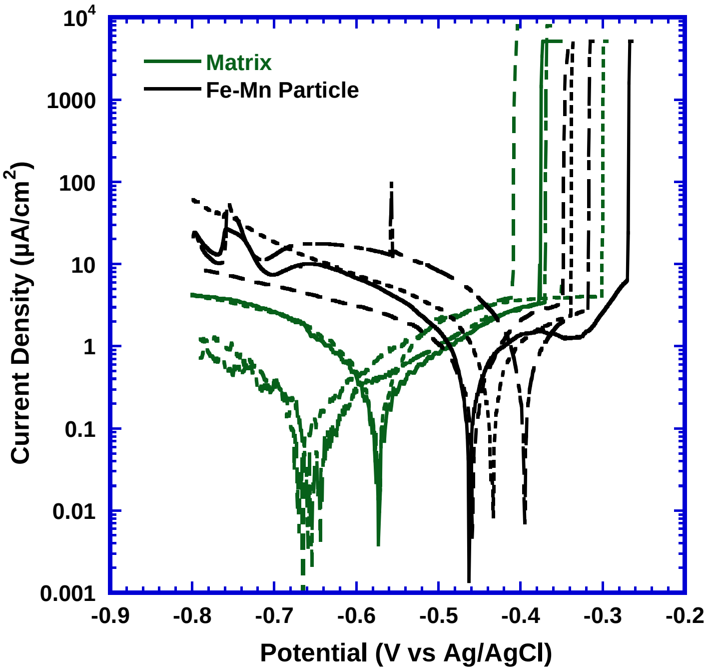

Figure 5.2 Comparison of anodic polarization curves of Fe-Mn particles and matrix of AA2024-T351 in naturally aerated 0.1 M NaCl measured using capillary of 40 μm diameter. Scan start potential was -800 mV vs. Ag/AgCl with a scan rate of 1 mV/s.

It has to be noted that, anodic polarization scans on ‘S’ phase particles could not be performed from -800 mV vs. Ag/AgCl as it showed positive current directly indicating instant dissolution of that phase. It can be seen from Figure 5.2 that the cathodic reactivity of the Fe-Mn particles is still higher than the matrix. Corrosion potentials of the Fe-Mn particles are between -475 to -400 mV vs. Ag/AgCl whereas breakdown potentials are between -350 to 300 mV vs. Ag/AgCl. Fe-Mn particles from different AA2024-T351 samples behave almost similarly, however sometime slight differences have been noticed in the matrix cathodic-reactivity of two repeat samples (Figure 5.2). Matrix of one sample shows lower cathodic reactivity (~1 µA/cm^2) and lower corrosion potential (~-660 mV vs. Ag/AgCl) than the other (~5 µA/cm^2 and -580 mV vs. Ag/AgCl respectively). This difference could be associated with the inherent variability of the aluminium alloys though all samples are prepared following exactly similar procedure.

Figure 5.3 shows the comparison of the anodic polarization scans of the matrix and Fe-Mn particles when the scans were started at -700 mV vs. Ag/AgCl. Experimental conditions and parameters for the potentiodynamic scans of Figure 5.3 were similar to that of Figure 5.1 and Figure 5.2 except for the scan start potential. It is interesting to note that in this case, both matrix and Fe-Mn particles show similar cathodic reactivity and corrosion potential. However, the average breakdown potential (-300 mV vs. Ag/AgCl) of the matrix is higher than the Fe-Mn particles (-400 mV vs. Ag/AgCl). For both scan start potentials of -1000 mV and -800 mV vs. Ag/AgCl, ‘S’ phase particles and Fe-Mn particles always showed higher cathodic reactivity than the matrix.

Figure 5.4 and Figure 5.5 show the summary of the breakdown and corrosion potentials, respectively, of different phases as measured from the anodic polarization scans started at different cathodic potentials. Figure 5.4 shows that the ‘S’ phase particles have the lowest breakdown potentials between -600 to -700 mV vs. Ag/AgCl. The scatter of the breakdown potential for matrix scanned from -1000 mV vs. Ag/AgCl is between -280 to -460 mV vs. Ag/AgCl with only one case where the breakdown potential is as high as 0 mV vs. Ag/AgCl. For Fe-Mn particles, scans from -800 vs. Ag/AgCl shows lower breakdown potentials compare to the -1000 mV scans. At the scan start potential of -700 mV vs. Ag/AgCl, breakdown potential of the matrix is slightly higher than the Fe-Mn particle in most of the cases.

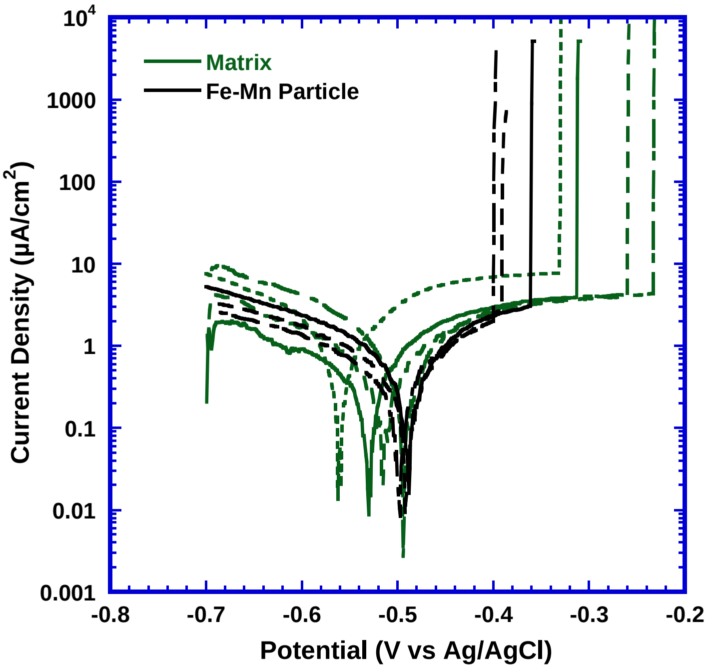

Figure 5.3 Comparison of anodic polarization curves of Fe-Mn particles and matrix of AA2024-T351 in naturally aerated 0.1 M NaCl measured using capillary of 40 µm diameter. Scan start potential was -700 mV vs. Ag/AgCl with a scan rate of 1 mV/s.

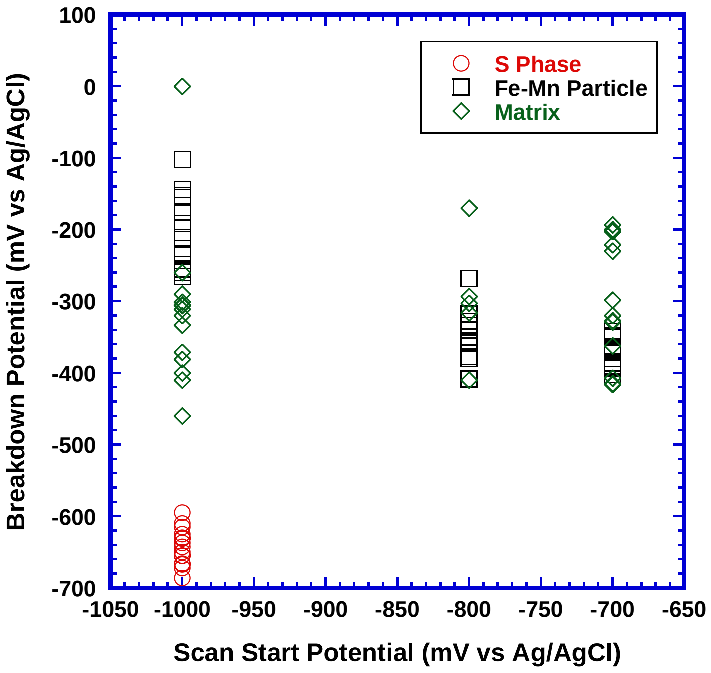

Figure 5.4 Comparison of the breakdown potentials of 'S' phase particles, Fe-Mn particles and matrix of AA2024-T351 in naturally aerated 0.1 M NaCl as a function of different scan start potential as measured during the potentiodynamic scans using capillary of 40 µm diameter.

It can be seen from Figure 5.5 that when the scans started at -1000 mV or at -800 mV vs. Ag/AgCl, Fe-Mn particles have higher corrosion potentials than the 'S' phase particles and the matrix. At all scan start potentials, the scatter of corrosion potentials of different phases are between 100-150 mV. This could be due to the inherent local inhomogeneity of the aluminium alloys in combination with the very small exposure area of 40 micron diameter.

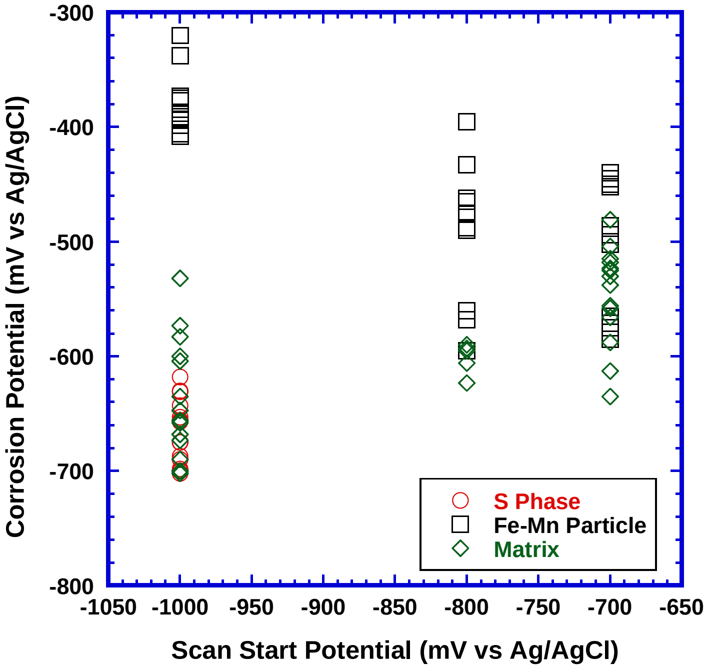

Figure 5.5 Comparison of the corrosion potentials of 'S' phase particles, Fe-Mn particles and matrix of AA2024-T351 in naturally aerated 0.1 M NaCl as a function of different scan start potential as measured during the potentiodynamic scans using a 40 μm diameter capillary.

Optical images of the Fe-Mn particles before and after the potentiodynamic tests from different scan start potentials are shown in Figure 5.6 and Figure 5.7. Two Fe-Mn particles with different shapes before and after potentiodynamic tests from -1000 mV vs. Ag/AgCl are shown in Figure 5.6. These two particles are the representative from several other potentiodynamic scans on Fe-Mn particles staring from -1000 mV. In all cases Fe-

Mn particles turned black. The composition of the black layer is not known, but it could not be removed even after ultrasonic cleaning in ethanol.

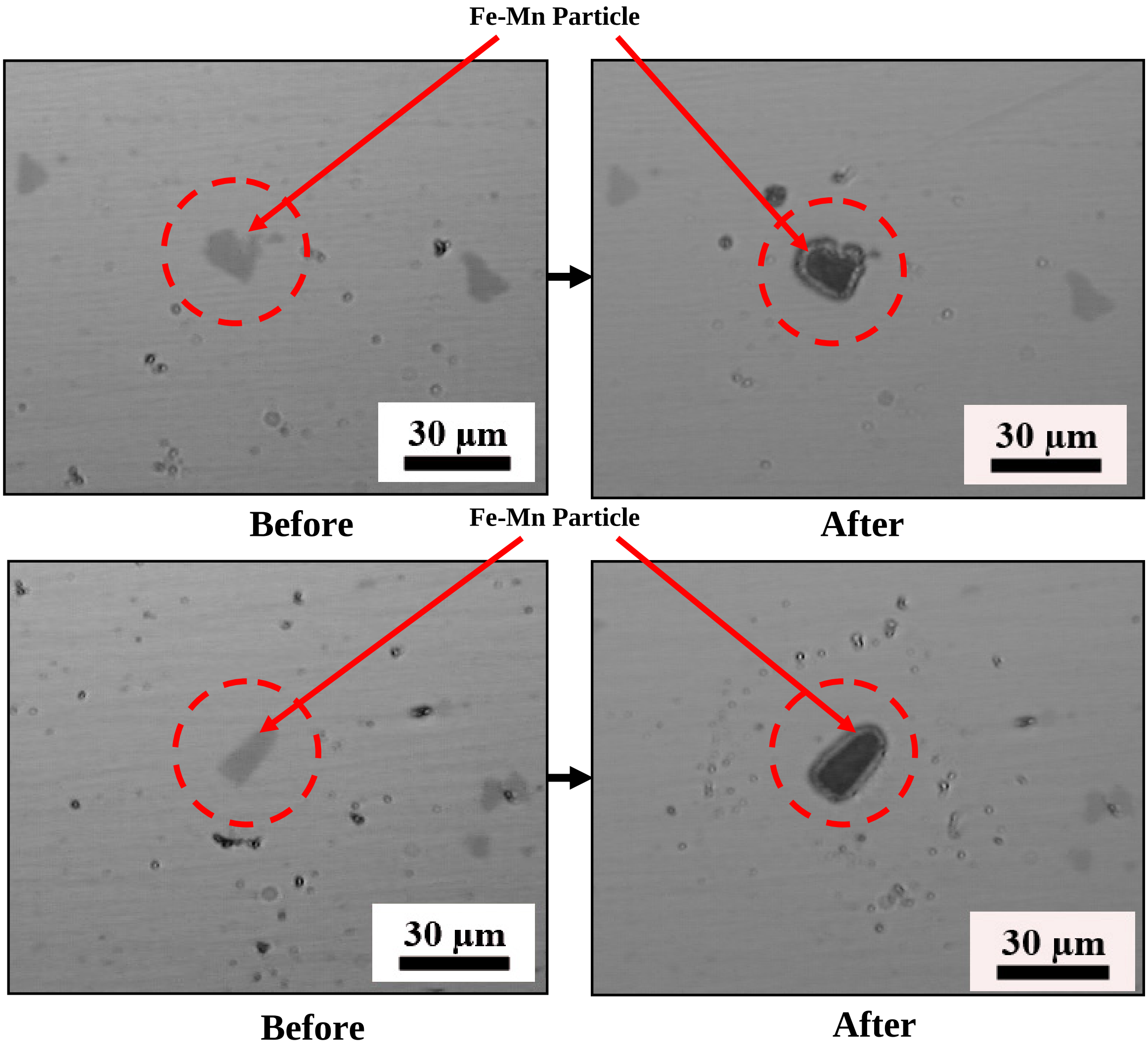

Figure 5.6 Optical images of the Fe-Mn particles before and after an anodic polarization scan from -1000 mV vs. Ag/AgCl in naturally aerated 0.1 M NaCl (40 µm diameter capillary, scan rate = 1 mV/s). Particle turned black after the polarization scan.

However, Figure 5.7 shows that when the potentiodynamic scans on Fe-Mn particles were performed from -700 mV vs. Ag/AgCl, presence of any black layer was not observed. Several Fe-Mn particles were analyzed in this manner which leads to consistent findings.

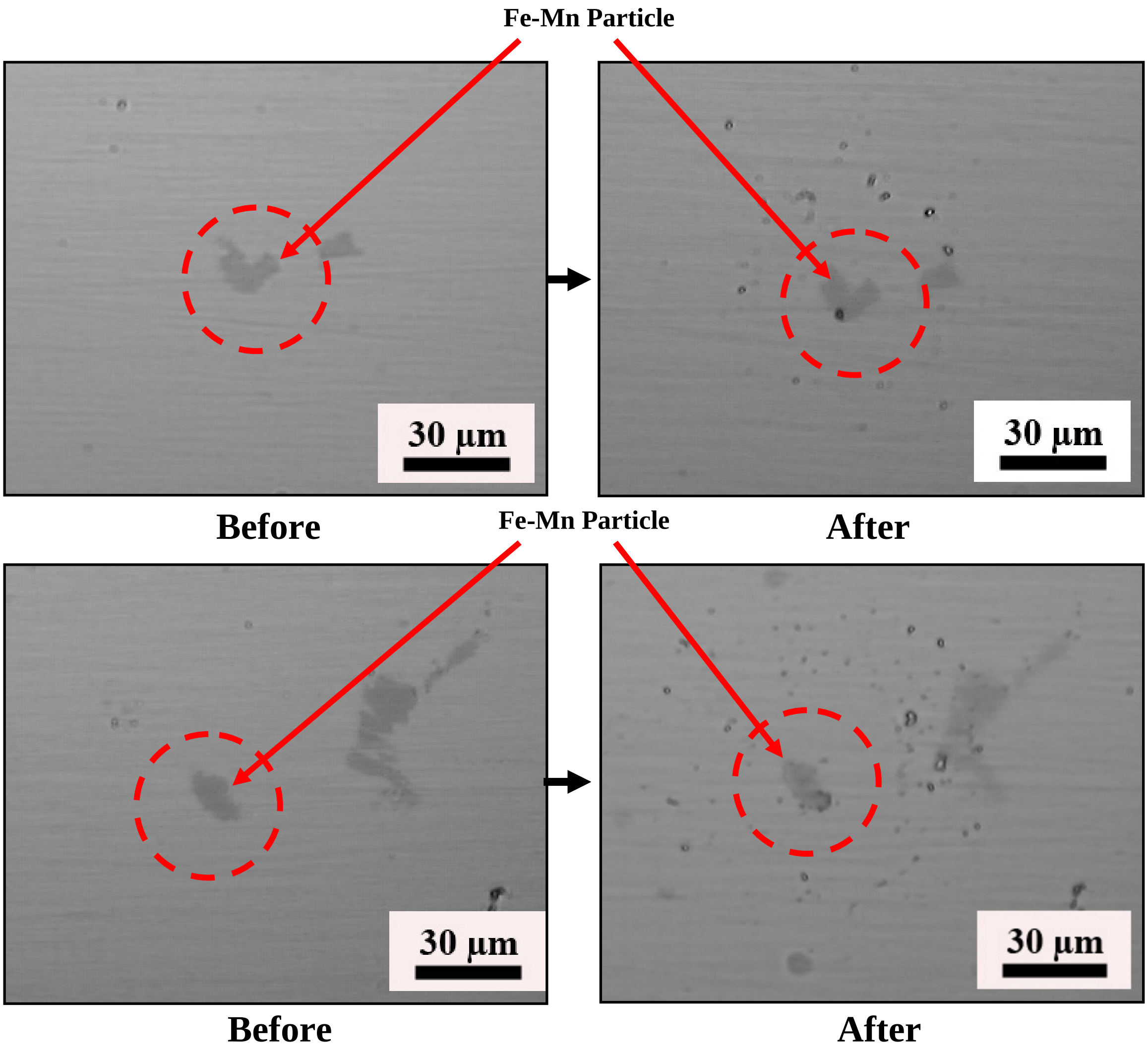

Figure 5.7 Optical images of the Fe-Mn particles before and after the anodic polarization scan from -700 mV vs. Ag/AgCl in naturally aerated 0.1 M NaCl (40 µm diameter capillary, scan rate = 1 mV/s). After the polarization scan, particle appearance did not change, i.e., particle did not turn black.

Potentiodynamic scans on Fe-Mn particles from -800 mV vs. Ag/AgCl also do not show any change in the sample appearance expect in one or two cases where the particle turns black. Interestingly, the potentiodynamic scan from -800 mV vs. Ag/AgCl resulting in a black layer on the Fe-Mn particle looks similar to the -1000 mV vs. Ag/AgCl scan (i.e., scan shows a higher corrosion and breakdown potential compare to the other -800 mV vs. Ag/AgCl scans). This confirms the role of any surface modification during the scans from -1000 mV vs. Ag/AgCl thereby yielding higher corrosion and breakdown potentials. A thick silicone coating at the capillary tip helped to avoid the formation of crevices at the capillary edge or any indentation in the surface.

Figure 5.8, Figure 5.9, and Figure 5.10 show SEM images of the morphology of Fe-Mn particles before and after the anodic potentiodynamic scans from different starting potentials. When the scans were started at -700 mV vs. Ag/AgCl, pitting attacks were observed in the particle (Figure 5.8a) and in both particle and the matrix (Figure 5.8b).

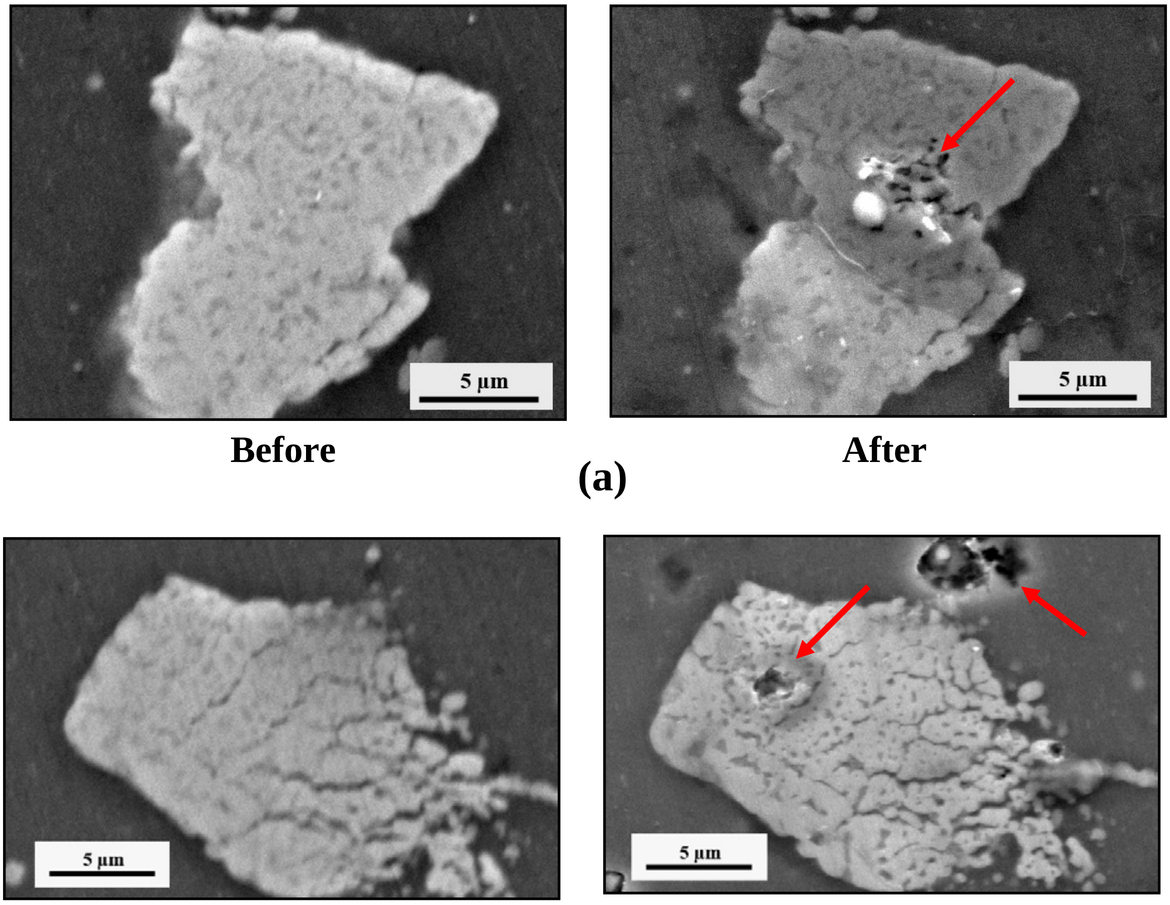

Before **After**

(a)

Before **After**

(b)

Figure 5.8 SEM images of Fe-Mn particle before and after the anodic polarization scan from -700 mV vs. Ag/AgCl in naturally aerated 0.1 M NaCl (40 µm diameter capillary, scan rate = 1 mV/s). (a) Pitting attack has been observed in the particle after the test. (b) Pitting attack has been observed both in the particle and in the adjacent matrix.

Figure 5.9a shows the initiation of pitting at the edge of the particle when the scan started at -800 mV vs. Ag/AgCl. However, pitting can also be observed on the particle itself when potentiodynamic scan started at the same potential, Figure 5.9b.

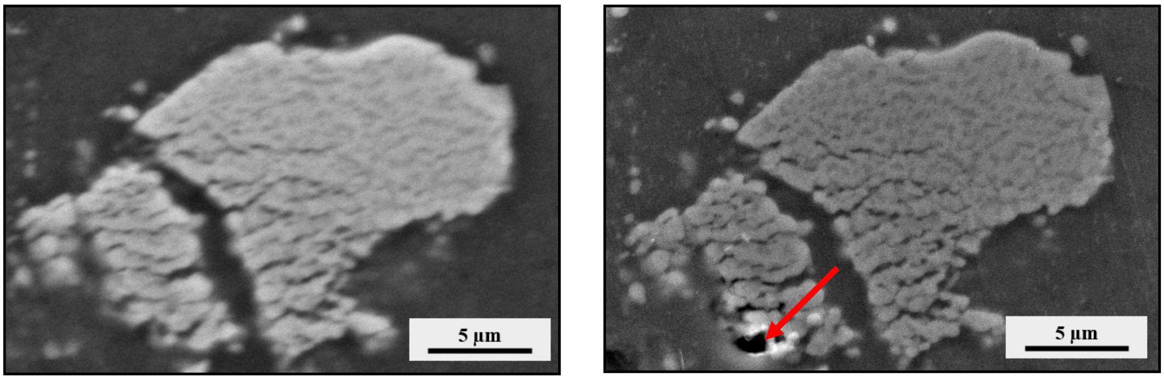

Before **(a)** **After**

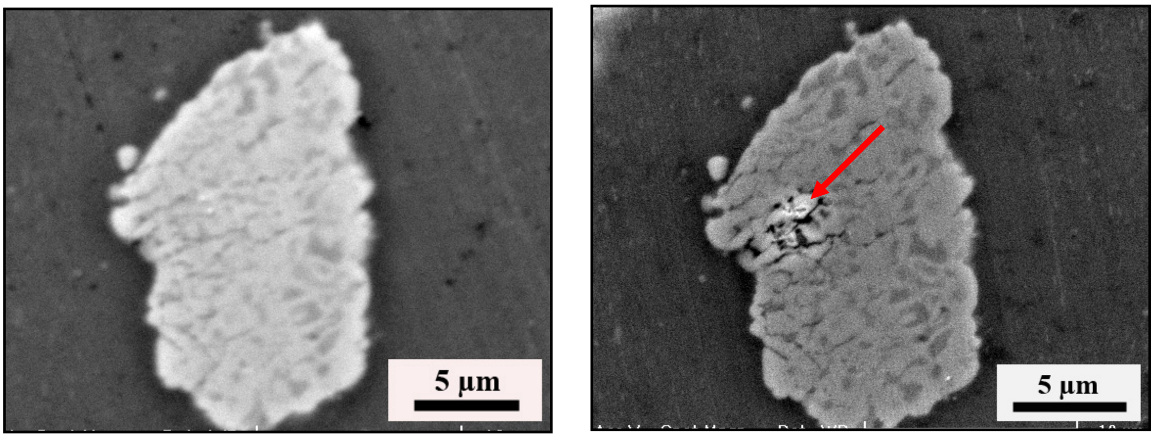

Before **(b)** **After**

Figure 5.9 SEM images of Fe-Mn particle before and after the anodic polarization scan from -800 mV vs. Ag/AgCl in naturally aerated 0.1 M NaCl (40 µm diameter capillary, scan rate = 1 mV/s). (a) Pitting initiated at the edge of the particle. (b) Initiation of pitting attack can be seen on the particle itself.

When the scan was started at -1000 mV vs. Ag/AgCl, pitting attack was seen in the matrix adjacent to the particle (Figure 5.10a) and at the edge of the particle (Figure 5.10b). Analyzing all the SEM images for the pit initiation sites after the potentiodynamic scans, it is difficult to correlate any particular type of initiation site with any particular scan start potential. All that can be concluded is that pits can initiate in the particle itself, at the particle edge, in the adjacent matrix or in both particle and matrix.

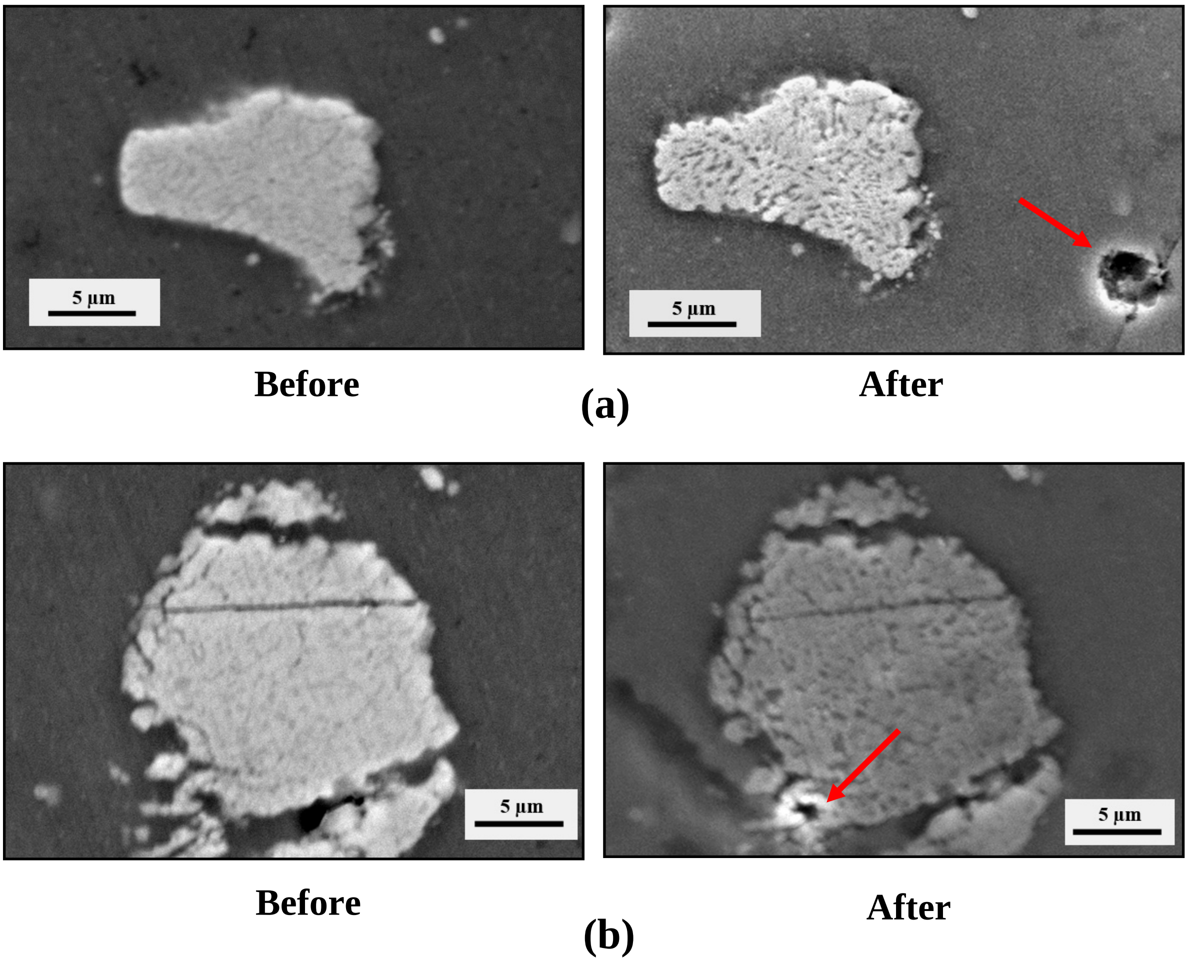

Figure 5.10 SEM images of Fe-Mn particle before and after the anodic polarization scan from -1000 mV vs. Ag/AgCl in naturally aerated 0.1 M NaCl (40 µm diameter capillary, scan rate = 1 mV/s). (a) Particle remained unattacked whereas pitting initiated at the matrix. (b) Pitting initiated at the edge of the particle.

Figure 5.11 shows the morphology of the ‘S’ phase particles before and after the potentiodynamic tests when the scans were started from -1000 mV vs. Ag/AgCl. It is not surprising that no severe dissolution or localized attacks are observed in these exposed ‘S’ phase particles. For all ‘S’ phase particles, scans were stopped right after the current reached the value of 10 nA. As the current increases sharply right after the corrosion potential and the scans were stopped at very low current, extensive dissolution or localized attack growth was not possible. However, slight grooving adjacent to some part of the exposed ‘S’ phase particles and slight etching of the particles was observed.

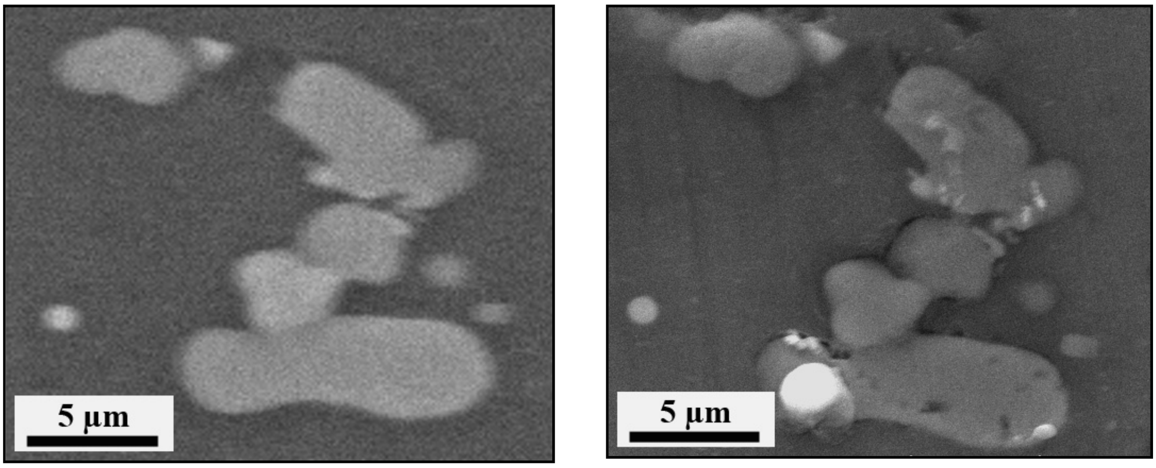

Before **After**

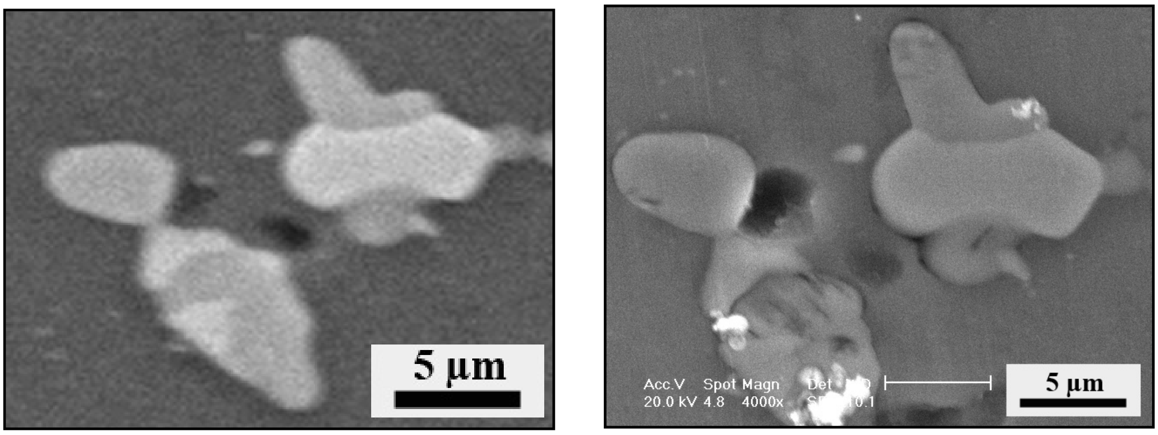

Before **After**

Figure 5.11 Typical SEM images of ‘S’ phase particles before and after the anodic polarization scans from -1000 mV vs. Ag/AgCl in naturally aerated 0.1 M NaCl (40 µm diameter capillary, scan rate = 1 mV/s).

Figure 5.12 and Figure 5.13 show the typical attack morphology on the matrix of AA2024-T351 after the anodic potentiodynamic scans were performed in 0.1 M NaCl from starting potentials of -700 mV and -1000 mV vs. Ag/AgCl respectively. No obvious differences in the attack morphology on the matrix as a function of scan start potential were observed. All the attacks are identified as pitting.

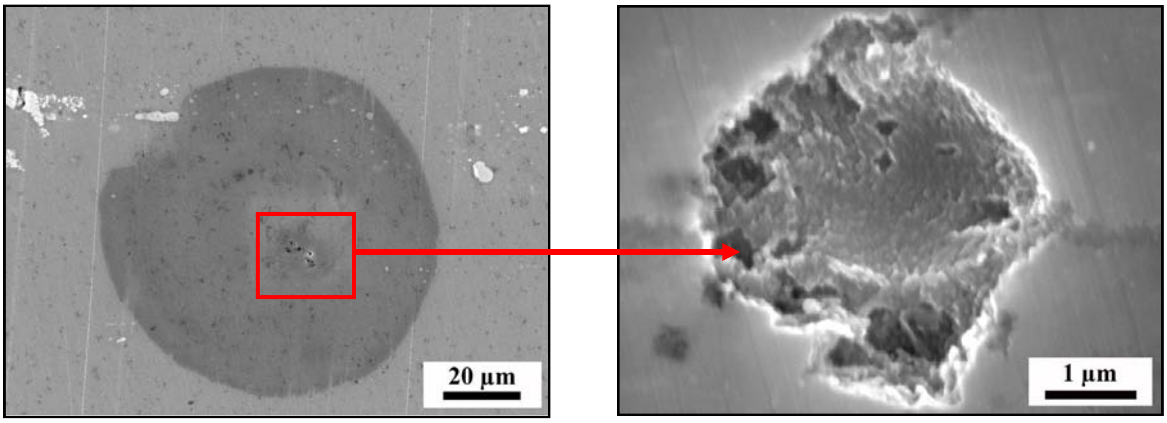

Figure 5.12 SEM images of a typical localized attack morphology in the matrix after anodic polarization scan from -700 mV vs. Ag/AgCl in naturally aerated 0.1 M NaCl (40 μm diameter capillary, scan rate = 1 mV/s). Internal surfaces of this hemispherical pit are composed of crystallographic corrosion facets.

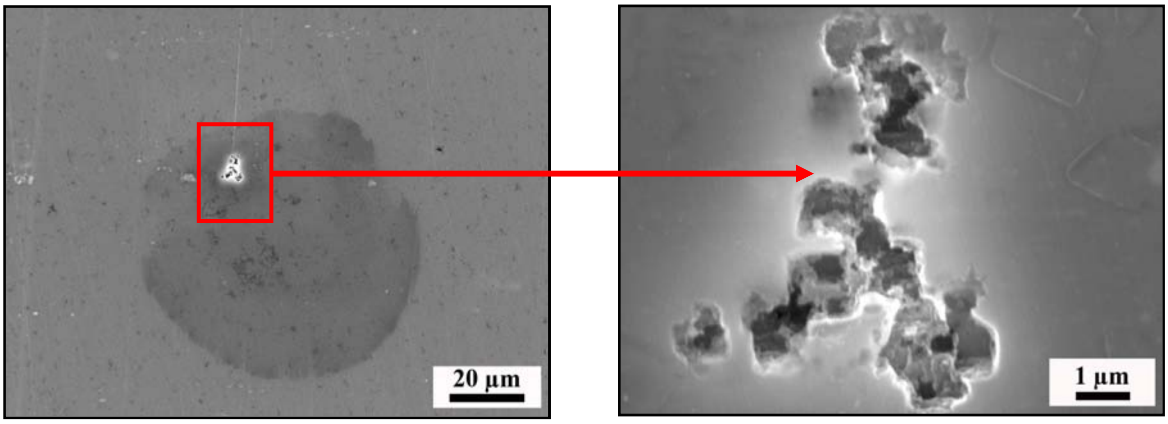

Figure 5.13 SEM images of a typical localized attack morphology in the matrix after anodic polarization scan from -1000 mV vs. Ag/AgCl in naturally aerated 0.1 M NaCl (40 μm diameter capillary, scan rate = 1 mV/s). Internal surfaces of the pitting attack are seemed to compose of crystallographic corrosion tunnels.

Typical pits were in the size range of 4-5 µm in diameter (Figure 5.12) and sometime several small pits clustered together and crystallographic facets were found at the inside wall of the pit (Figure 5.13).

Figure 5.14 shows a few potentiodynamic scans on the Fe-Mn particles carried out in naturally aerated 0.5 M NaCl from -955 mV vs. Ag/AgCl (i.e., -1000 mV vs. SCE). Potentiodynamic scans were stopped just before reaching the corrosion potential, before reaching the pitting potential, and just after pitting. The idea was to perform morphological analyses of the exposed Fe-Mn particle using optical profilometry to find out if the nature/morphology of the grooving changes in the anodic domain. Another objective of these experiments was to investigate the effect of higher chloride concentration on the corrosion behaviour of the particles. Potentiodynamic scans from -955 mV vs. Ag/AgCl on Fe-Mn particles in 0.5 M NaCl are quite similar to the scans performed in 0.1 M NaCl from -1000 mV vs. Ag/AgCl (see Figure 5.1). Cathodic reactivity and corrosion potential of Fe-Mn particles remain similar in both concentrations of sodium chloride solution. However, breakdown potential of Fe-Mn particles are slightly lower (~-270 mV vs. Ag/AgCl) in 0.5 M NaCl than in 0.1 M NaCl (~-200 mV vs. Ag/AgCl). It is hence reasonable to conclude that increase in the aggressiveness of the solution cause the lowering of the breakdown potential. It is interesting to note that, although the potentiodynamic tests were started at the same cathodic potentials and stopped at different potential (i.e., before reaching the corrosion potential or in the anodic domain), in all three cases particles turned black. This confirms that the blackening of the particle is due to the cathodic polarization and not related to the pitting.

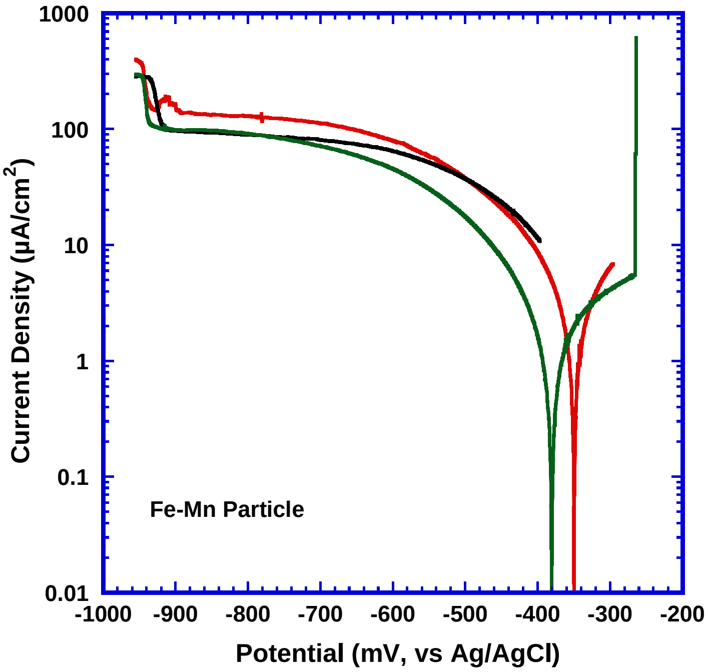

Figure 5.14 Comparison of potentiodynamic polarization curves of Fe-Mn particles of AA2024-T351 in naturally aerated 0.5 M NaCl (40 µm diameter capillary, scan rate = 1 mV/s). Scan start potential was -955 mV vs. Ag/AgCl. Scans were stopped before reaching to the corrosion potential, before reaching the pitting potential and just after pitting.

Optical profilometric analysis was performed to determine the extent/nature of grooving around the particles and to get more details of the surface topography of the particles and their surroundings after the test. Samples were ultrasonically cleaned in ethanol for 4 min before the profilometric study. This helped to remove all the NaCl crystals deposited on the surface during the test.

Figure 5.15 and Figure 5.16 clearly establish the presence of a groove around the Fe-Mn particle as well as attack on the particle itself. Figure 5.15 shows the surface topography of the particle and surrounding matrix after the potentiodynamic scan (from -1000 mV vs. SCE) was stopped just before pitting. This figure clearly shows the groove around the particle and the partial dissolution of the particle. The depth profilometry reveals that the groove around the particle is about 6-10 µm wide and ~ 6 µm deep in some places.

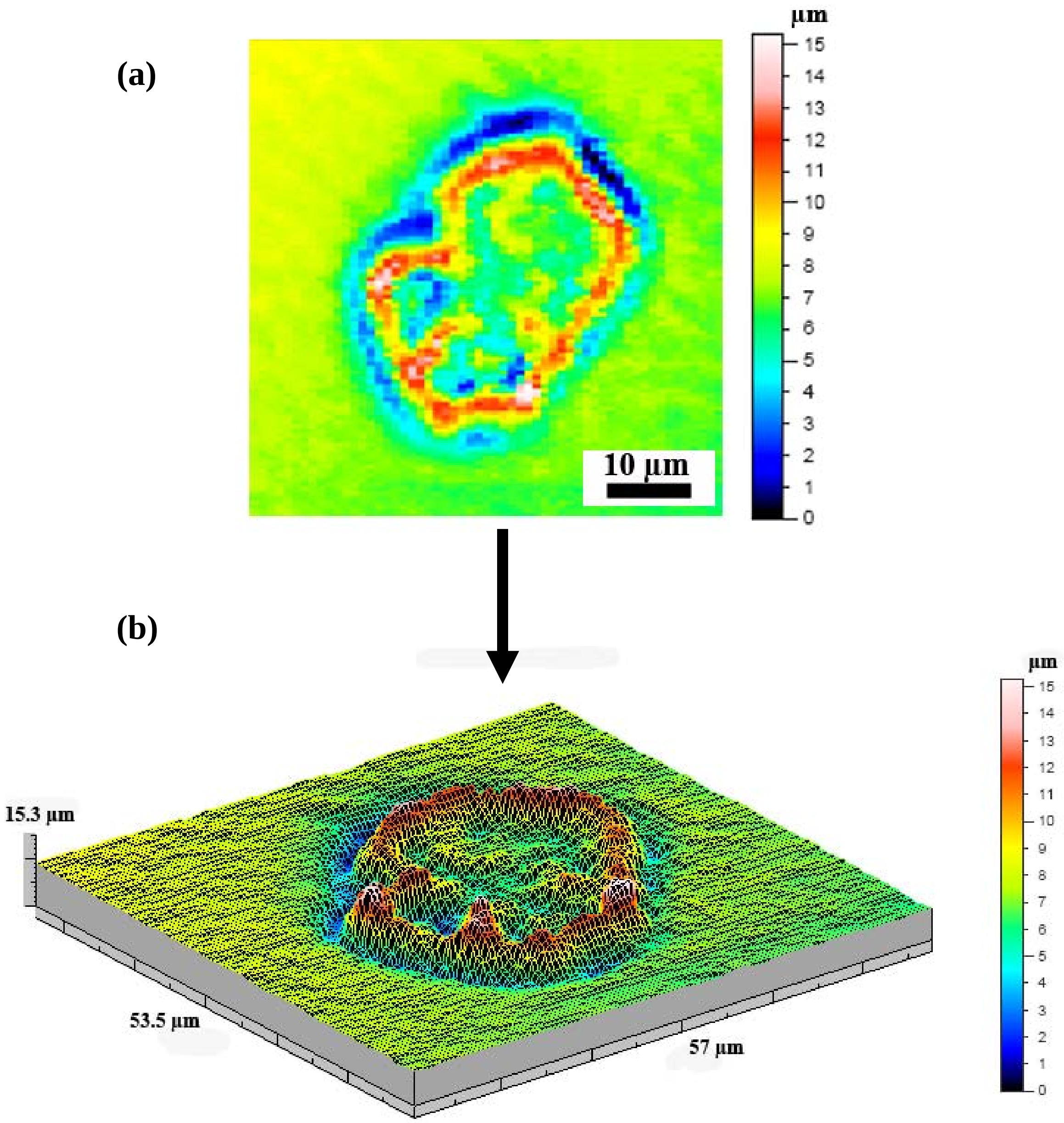

Figure 5.15 Optical profilometric analysis of a Fe-Mn particle showing the surface topography of the particle and the surrounding matrix after the anodic polarization scan from -955 mV vs. Ag/AgCl in naturally aerated 0.5 M NaCl (40 µm diameter capillary, scan rate = 1 mV/s). The scan (represented by the red curve in Figure 5.14) was stopped just before pitting.

Figure 5.16 shows the surface topography of the particle and surrounding matrix after the potentiodynamic scan from -1000 mV vs. SCE was stopped just after pitting. The small portion with maximum height (indicated as red) is probably a dust particle deposited on the surface. The grooving around the particle could be as wide as 10 µm with a maximum depth of 4 µm. Similar type of continuous and wide grooving around the particle (results not shown) has also been observed when the potentiodynamic scan was stopped before reaching the corrosion potential (i.e., the black curve in Figure 5.14).

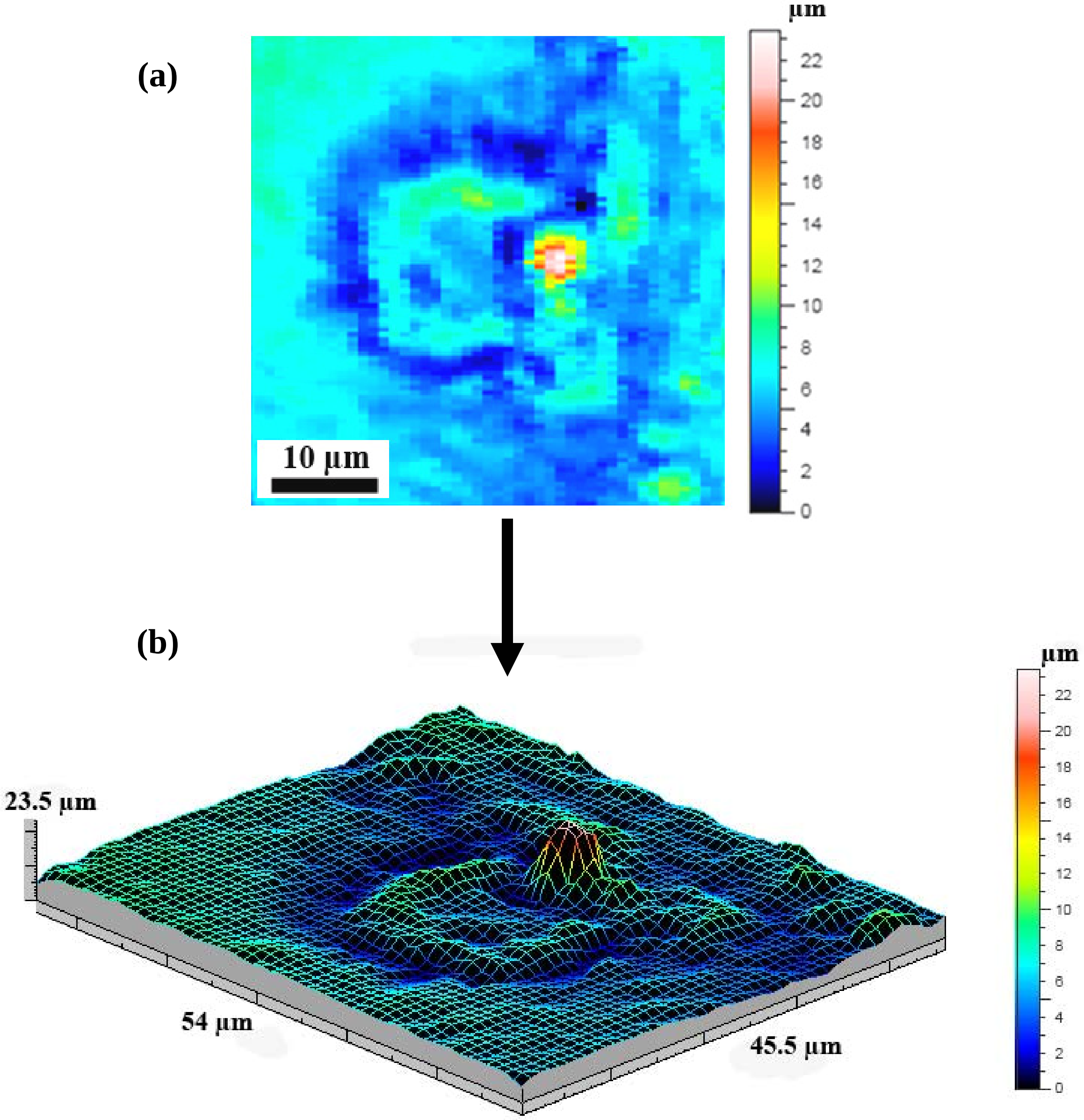

Figure 5.16 Optical profilometric analysis of a Fe-Mn particle showing the surface topography of the particle and the surrounding matrix after the anodic polarization scan from -955 mV vs. Ag/AgCl in naturally aerated 0.5 M NaCl (40 µm diameter capillary, scan rate = 1 mV/s). Scan (represented by the green curve in Figure 5.14) was stopped just after pitting.

Terminating the scan before pitting (Figure 5.15), just after pitting (Figure 5.16) or even before reaching the corrosion potential had little effect on the grooving around the particle. To confirm that these grooves were generated during the polarization scans and they did not pre-exist in the polished surface, profilometry of the particles without any electrochemical tests was carried out. The optical profilometer was not able to detect any topographic difference between the matrix and the Fe-Mn particle resulting from polishing.

Figure 5.17 shows the comparison of anodic polarisation scans on Fe-Mn particles in naturally aerated 0.1 M NaCl from different starting potentials.

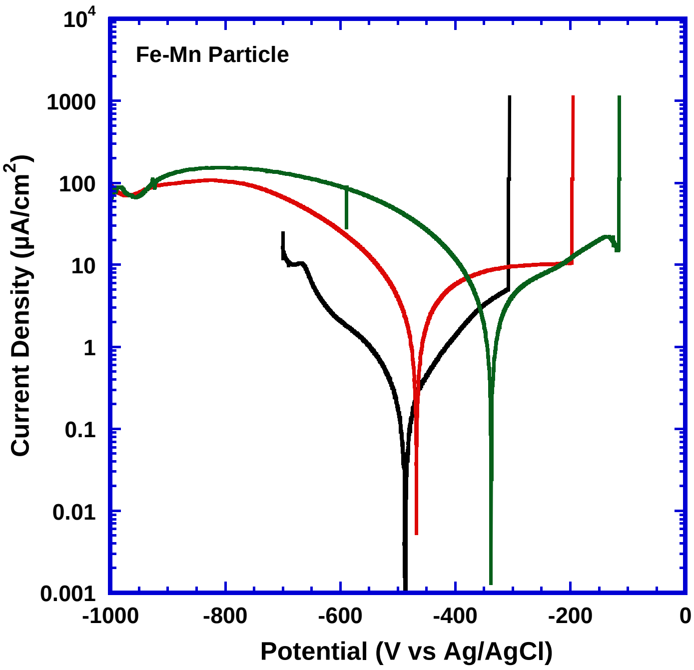

Figure 5.17 Comparison of anodic polarization curves of Fe-Mn particles of AA2024-T351 in naturally aerated 0.1 M NaCl measured using capillary of 40 µm diameter from different scan start potential at a scan rate of 1 mV/s.

These scans (shown in Figure 5.17) are selectively chosen as AFM analysis was performed on the particles after the test. The same trend can be observed here as it was seen in Figure 5.4 and Figure 5.5, i.e., a lower (more cathodic) scan starting potential leads to a higher OCP and breakdown potential. AFM could be more sensitive than the optical profilometer and hence able to detect very small pitting events. Apart from that, AFM studies also give much more details about the exact nature and the extent of grooving around the particle.

Figure 5.18 shows the presence of discontinuous grooving around the Fe-Mn particle. In some areas grooves are deeper than other areas. Appearance of continuous or discontinuous grooving around the particle could result from the compositional difference of the particle itself. Some Fe-Mn particles could have a copper rich outer skin which helps in providing better surface for oxygen reduction and hence promote adjacent matrix dissolution through increase in local alkalinity. It is interesting to note that optical profilometry on the Fe-Mn particle after the polarization scan to pitting in 0.5 M NaCl (see Figure 5.16) shows much wider spread of the continuous groove around the particle than the discontinuous grooving shown in Figure 5.18 (in 0.1 M NaCl) through AFM analysis. This possibly emphasizes the role of solution concentration on the corrosion behaviour of the particle as well.

Figure 5.19a shows the AFM images a particular Fe-Mn particle before the test and Figure 5.19b shows the same particle after the potentiodynamic test in naturally aerated 0.1 M NaCl from a scan start potential of -1000 mV vs. Ag/AgCl. An AFM image of the unexposed Fe-Mn particle shows the flatness of the surface and the height difference between the matrix and the particle surface is only few tens of nanometres. Partial grooving around the Fe-Mn particle can be seen from Figure 5.19b. Interestingly both Figure 5.18 and Figure 5.19 represent scans which were stopped just after the pitting. So, the partial attack around the particle in this case could well be due to acidic grooving in the anodic region.

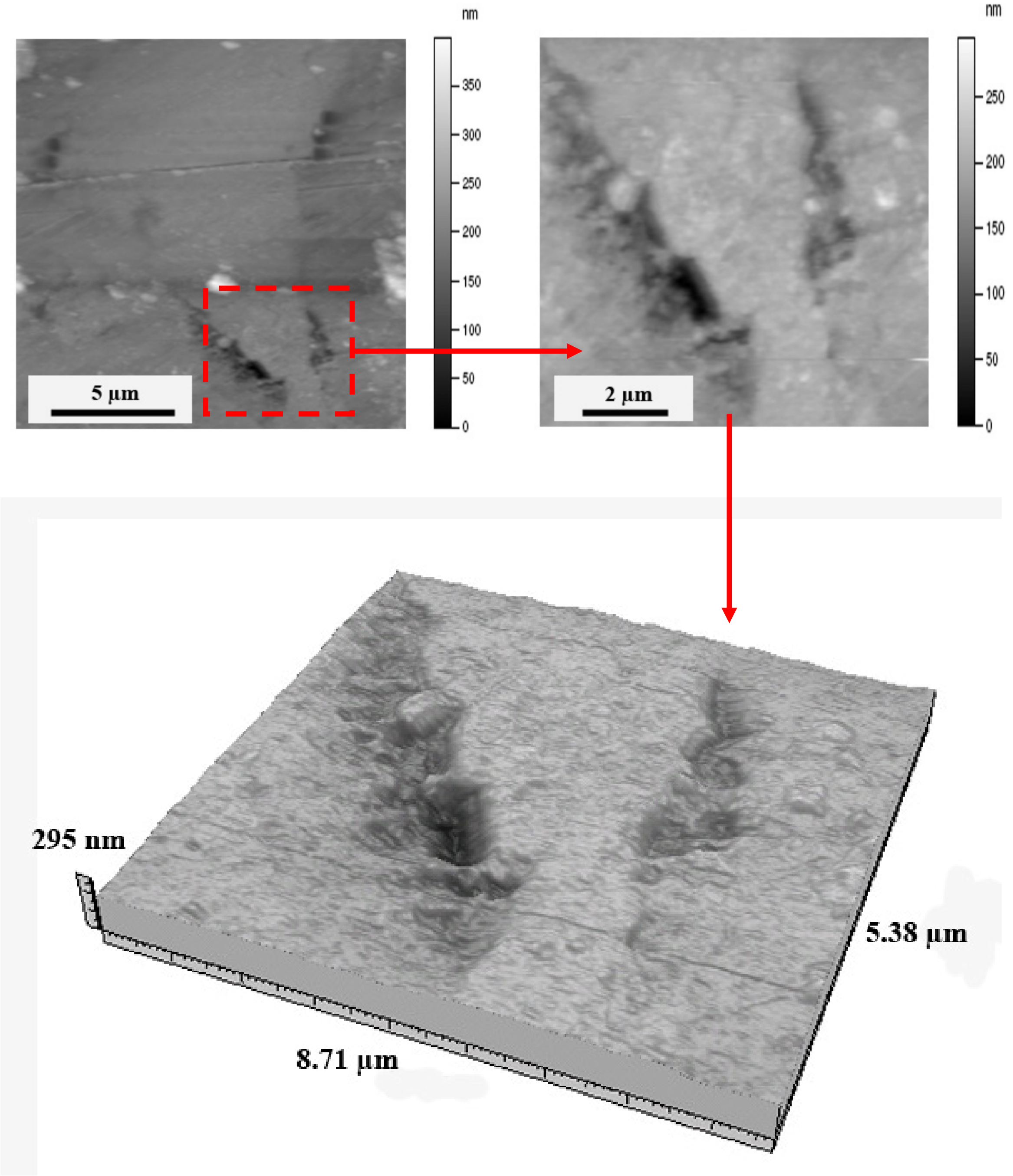

Figure 5.18 AFM images of a Fe-Mn particle after anodic polarization scan (represented by the red curve in Figure 5.17) from -1000 mV vs. Ag/AgCl till pitting (E_b ~ -194 mV) in naturally aerated 0.1 M NaCl at 1 mV/s using a capillary of 40 µm diameter. Discontinuous grooving around the particle has been observed.

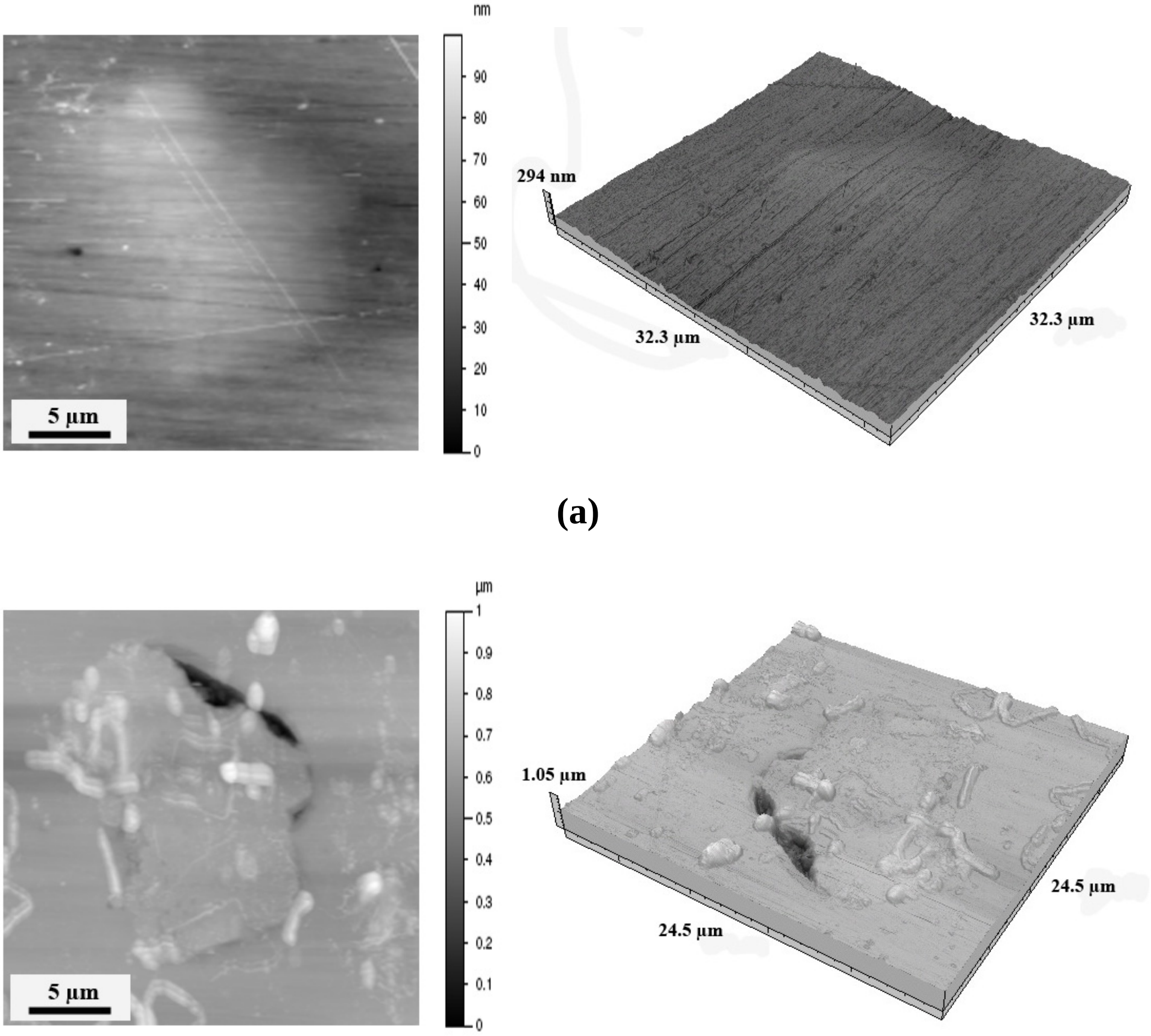

(a)

(b)

Figure 5.19 AFM images of a Fe-Mn particle; (a) before test, and (b) after anodic polarization scan (represented by the green curve in Figure 5.17) from -1000 mV vs. Ag/AgCl till pitting (E_b ~ -120 mV) in naturally aerated 0.1 M NaCl at 1 mV/s using a capillary of 40 µm diameter. Deep grooving has been observed at one side of the particle whereas the other edges do not show any presence of grooving.

Figure 5.20 shows the pitting attack at the edge of the particle when the scan was started from -700 mV vs. Ag/AgCl. It has to be noted that, none of the particles show grooving when the scans were started from -700 mV vs. Ag/AgCl.

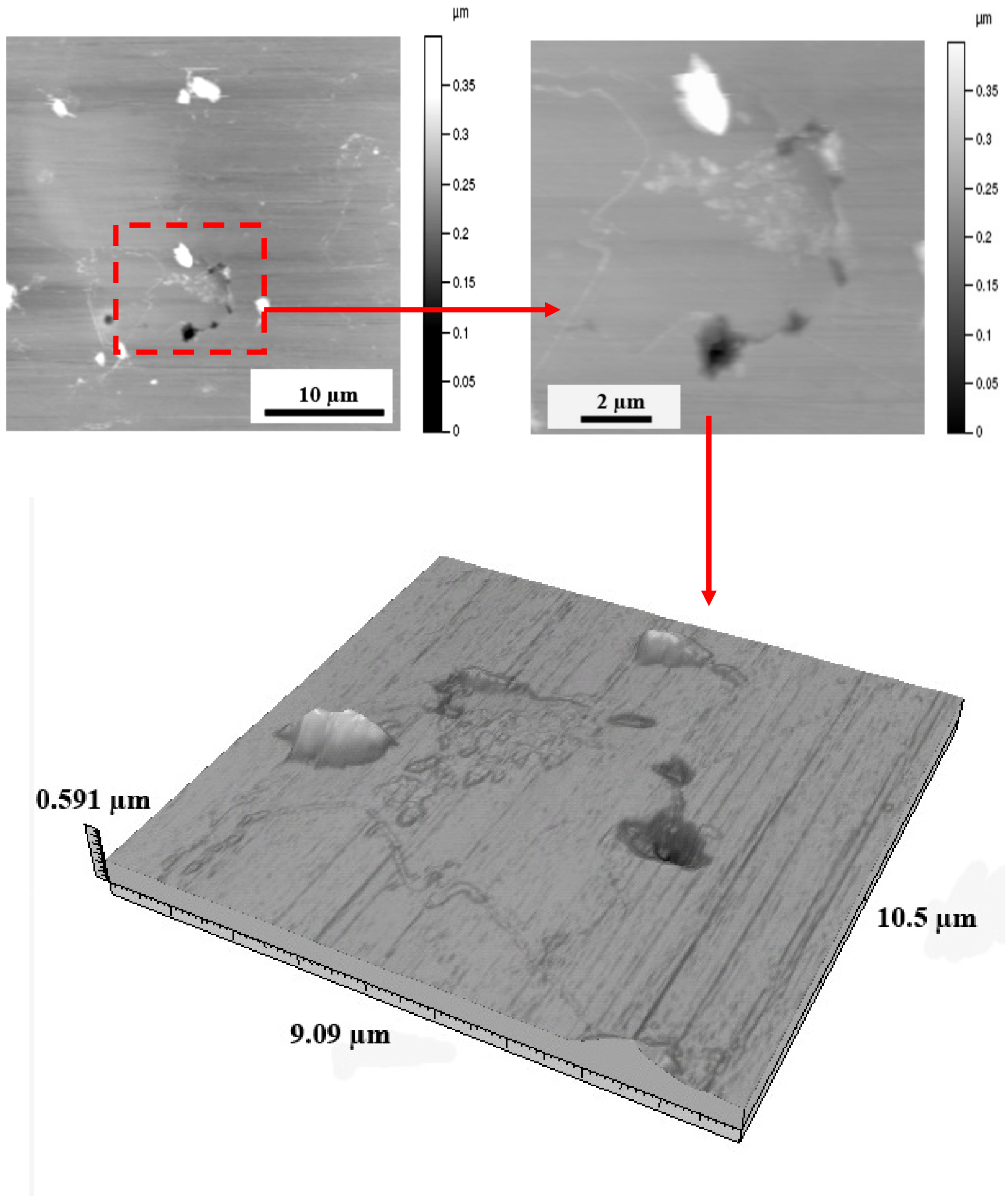

Figure 5.20 AFM images of a Fe-Mn particle after the anodic polarization scan (represented by the black curve in Figure 5.17) from -700 mV vs. Ag/AgCl till pitting (E_b ~ -306 mV) in naturally aerated 0.1 M NaCl at 1 mV/s using a capillary of 40 µm diameter. Only pitting has been observed at the edge of the particle.

Comparison of Figure 5.20 with Figure 5.18 and Figure 5.19 suggests that the discontinuous grooving around the Fe-Mn particles as seen in the scans from -1000 mV vs. Ag/AgCl may not result from the acidic grooving (or pitting). If it is caused by acidic grooving in the anodic region, the same type of attack morphology would have been seen in the scans from -700 mV vs. Ag/AgCl. So, the grooving may have caused by the increase in the local alkalinity during its stay in the long cathodic portion of the potentiodynamic scans.

Figure 5.21 shows the comparison of the potentiodynamic polarisation scans on Fe-Mn particles starting from -1000 mV vs. Ag/AgCl in naturally aerated 0.1 M NaCl but stopped before reaching the pitting potential. The idea was to perform AFM scans on the particles to find out if the nature/morphology of the grooving changes in the anodic domain (i.e., anodic portion of the potentiodynamic polarization scan). These experiments are quite similar to those described in Figure 5.14 with high chloride concentration (0.5 M NaCl).

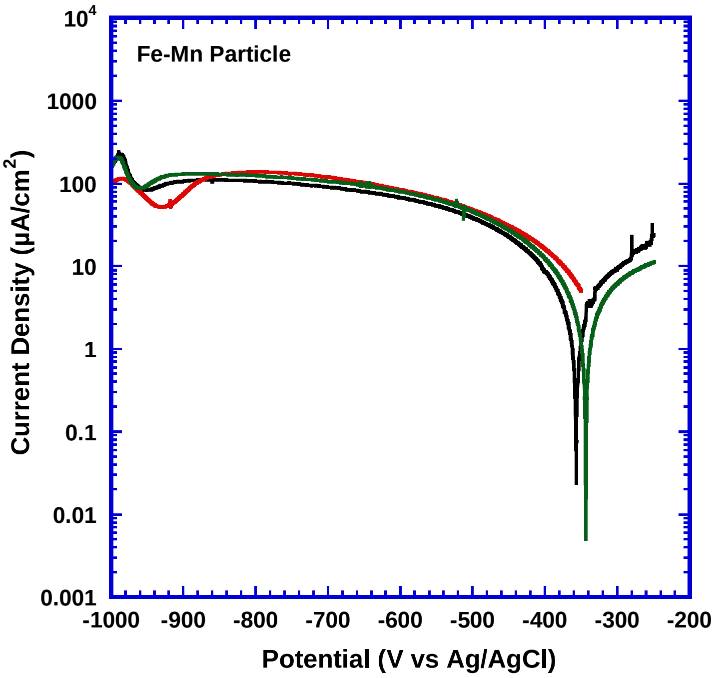

Figure 5.21 Comparison of potentiodynamic polarization curves of Fe-Mn particles of AA2024-T351 in naturally aerated 0.1 M NaCl measured using capillary of 40 µm diameter. Scan start potential was -1000 mV vs. Ag/AgCl with a scan rate of 1 mV/s and all of them were stopped before pitting.

Figure 5.22 shows a representative AFM scan on a Fe-Mn particle before and after the potentiodynamic test from -1000 mV vs. Ag/AgCl. In this case the scan was stopped at -250 mV vs. Ag/AgCl which is below the pitting potential.

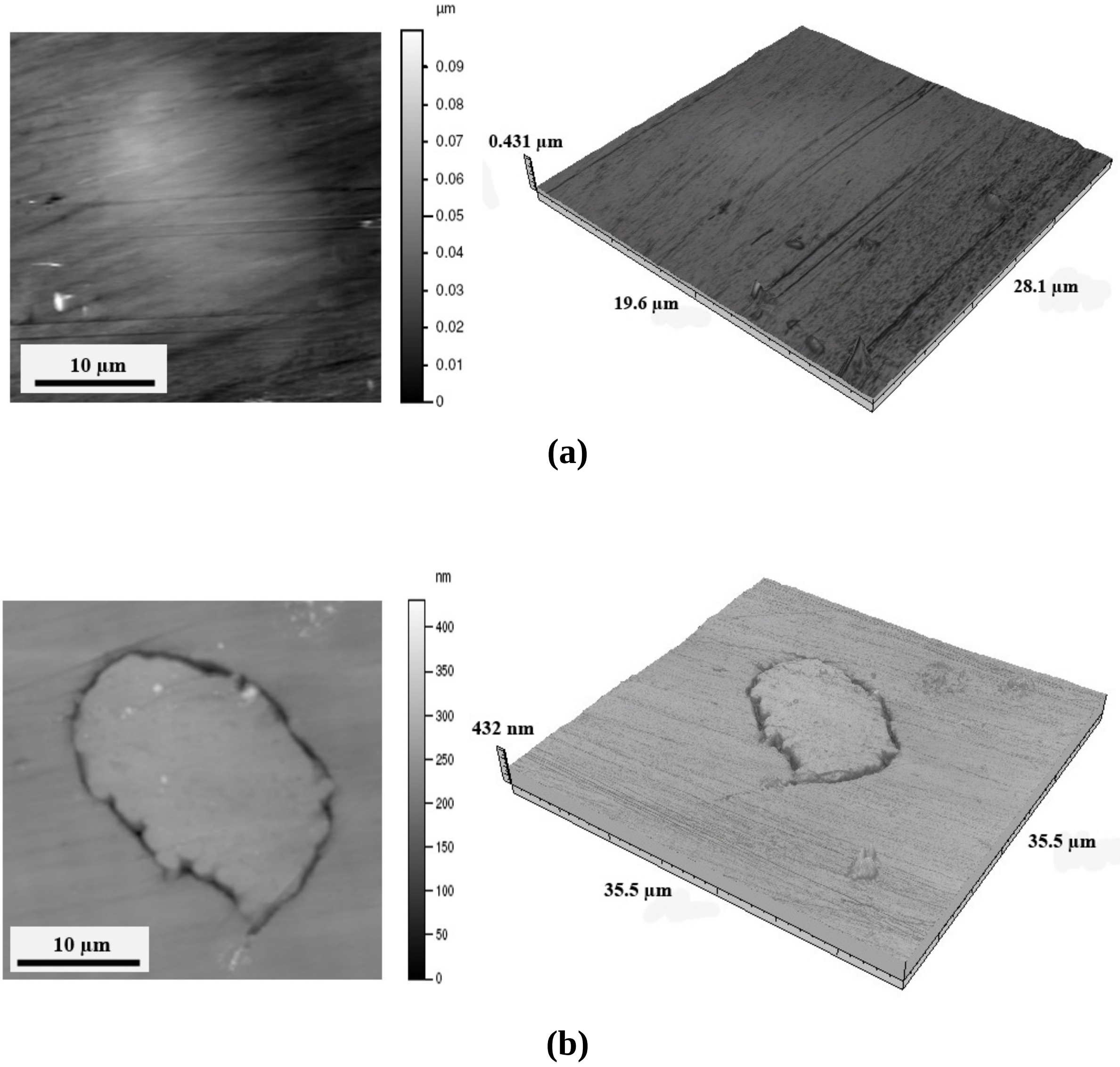

Figure 5.22 AFM images of a Fe-Mn particle; (a) before test, and (b) after anodic polarization scan (represented by the black curve in Figure 5.21) from -1000 mV vs. Ag/AgCl in naturally aerated 0.1 M NaCl at 1 mV/s. Scan was stopped in the anodic region (at -250 mV) before reaching to the pitting potential. Continuous grooving around the particle can easily be seen from the AFM image.

Figure 5.22b shows the grooving around the particle. Terminating the test before reaching the open circuit potential or before reaching the pitting potential does not have any effect on the appearance of the grooving. In all the cases continuous grooving around the particle is observed.

A typical anodic polarization scan on the ‘S’ phase particle performed in naturally aerated 0.1 M NaCl is shown in Figure 5.23. This particular scan was not stopped during the initial rapid increase in the current right after the corrosion potential (Figure 5.1), rather it was kept running till 200 mV vs. Ag/AgCl. As shown earlier (Figure 5.11), aborting the scan right after the initial increase in the current do not reveal any significant attack on the particle or adjacent to the particle.

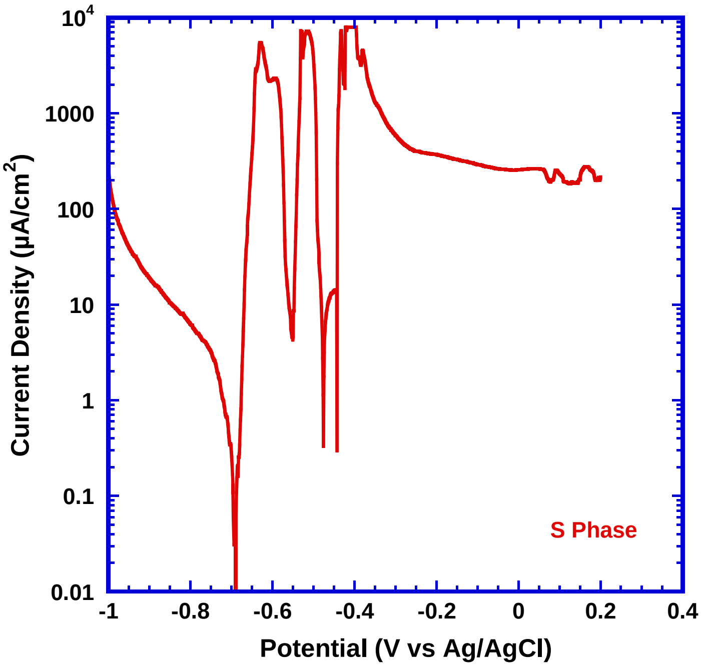

Figure 5.23 A typical anodic polarization curve of ‘S’ phase particle in naturally aerated 0.1 M NaCl (40 µm diameter capillary, scan rate = 1 mV/s). The scan was continued beyond the rapid increase in the current right after the corrosion potential.

However, when the scan was continued till 200 mV vs. Ag/AgCl, significant dissolution/attack on and around the particle can be seen, Figure 5.24. Initial rapid increases in the current are thought to be due to the selective dissolution of Mg from the 'S' phase particles. Once the selective dissolution of Mg from the particle is complete, current tend to decrease and become stable in the anodic region, Figure 5.23. SEM image of the 'S' phase particles clearly show the dissolution of the particles as well as some localized attack on the particles, Figure 5.24.

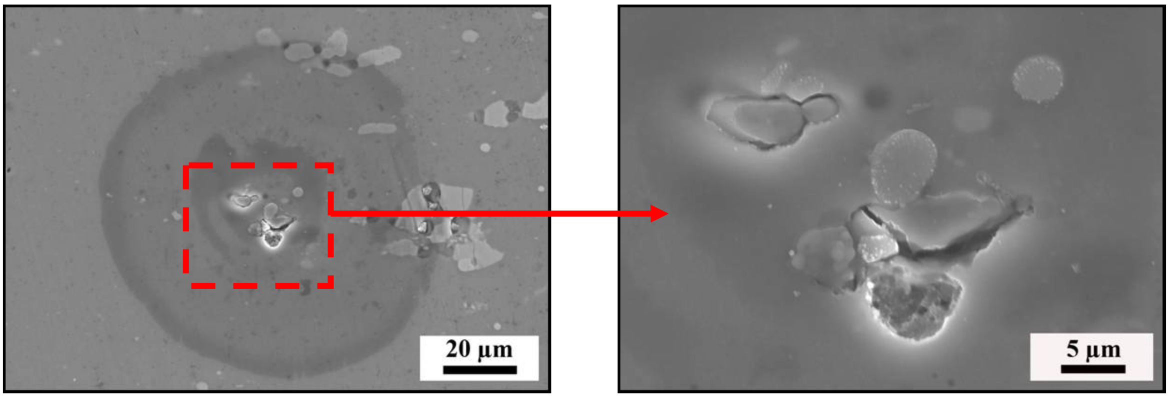

Figure 5.24 SEM images of exposed 'S' phase particles after the anodic polarization scan (shown in Figure 5.23) is continued till 200 mV vs. Ag/AgCl from the starting potential of -1000 mV vs. Ag/AgCl in naturally aerated 0.1 M NaCl (40 µm diameter capillary, scan rate = 1 mV/s). Longer potentiodynamic scans results into significant dissolution of 'S' phases.

5.2 Potentiostatic Polarization Measurements

Further experiments were performed on the intermetallic particles ('S' phase particles and Fe-Mn particles) of AA2024-T351 to compare their cathodic reactivity and to demonstrate the existence of alkaline grooving around the particle. Figure 5.25 shows the comparison of cathodic reactivity of Fe-Mn and 'S' phase particles as observed during potentiostatic polarization at -1000 mV vs. Ag/AgCl in naturally aerated 0.1 M NaCl. It was confirmed earlier that both particle behave cathodically at -1000 mV vs. Ag/AgCl (Figure 5.1). It is quite obvious from the figure that ‘S’ phase particles are more cathodically reactive than Fe-Mn particles. It is also interesting to note that cathodic current density increases for both types of particles as a function of time, but the rate of increase in the cathodic current for ‘S’ phase particles is more rapid compared to Fe-Mn particles. Eventually, after 10 minutes, the current in both cases seems to reach a plateau.

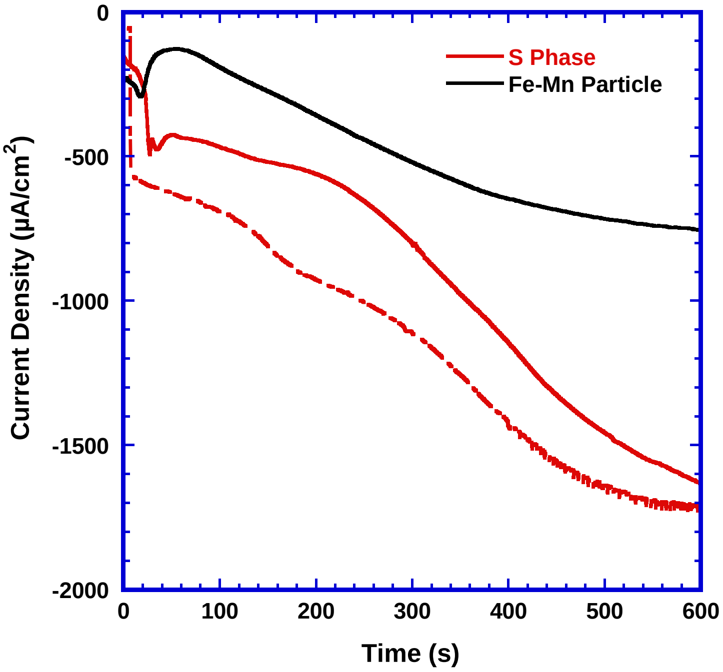

Figure 5.25 Potentiostatic polarization experiments on different particles of AA2024-T351 at E = -1000 mV vs. Ag/AgCl in naturally aerated 0.1 M NaCl (40 µm diameter capillary) in the cathodic domain. Cathodic current densities on the ‘S’ phase particles are higher than the current density of Fe-Mn particles.

Figure 5.26 shows a representative AFM scan of ‘S’ phase particle after the potentiostatic measurement in the cathodic domain. Alkaline grooving around the particle is quite clear. In most of the cases the grooves around the particles are continuous and deep. But in very few cases the grooving seems to spread out over larger area and discontinuous around the particle. These grooves around the particles are found to be few microns wide. Due to the constraint in the AFM tip geometry, depth measured by this technique might not be quite accurate.

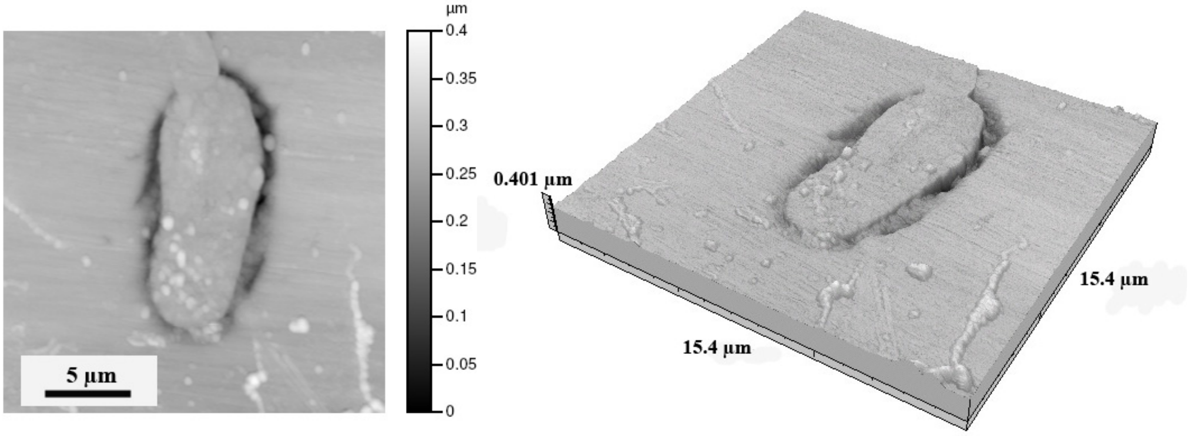

Figure 5.26 AFM images of ‘S’ phase particle after polarizing at a cathodic potential of -1000 mV vs. Ag/AgCl in naturally aerated 0.1 M NaCl for 10 minutes using a 40 μm diameter capillary. Current density as a function of time during the potentiostatic polarization of the ‘S’ phase particle is shown by the broken red line in Figure 5.25. Deep and continuous grooving in the matrix adjacent to the particle is observed.

Figure 5.27 shows AFM scan of a particular Fe-Mn particle before and after the cathodic potentiostatic test. AFM prior to the test reveals a smooth transition between the particle and matrix boundary and the height difference between the particle and matrix is only about 100 nm. Figure 5.27b shows continuous alkaline grooving around the particle. In all the cases alkaline grooving was found to be continuous.

Potentiostatic measurements on the ‘S’ phase particles and Fe-Mn particles were performed to find the current evolution as a function of time during the exposure. The potential (-600 mV vs. Ag/AgCl) was chosen in such a way that ‘S’ phase particles remain active at that potential (Figure 5.1). Figure 5.28 and Figure 5.29 shows the current vs. time on ‘S’ phase particles, Fe-Mn particles, and an area of mixed particle at a potential of -600 mV vs. Ag/AgCl for 15 minutes in naturally aerated 0.1 M NaCl.

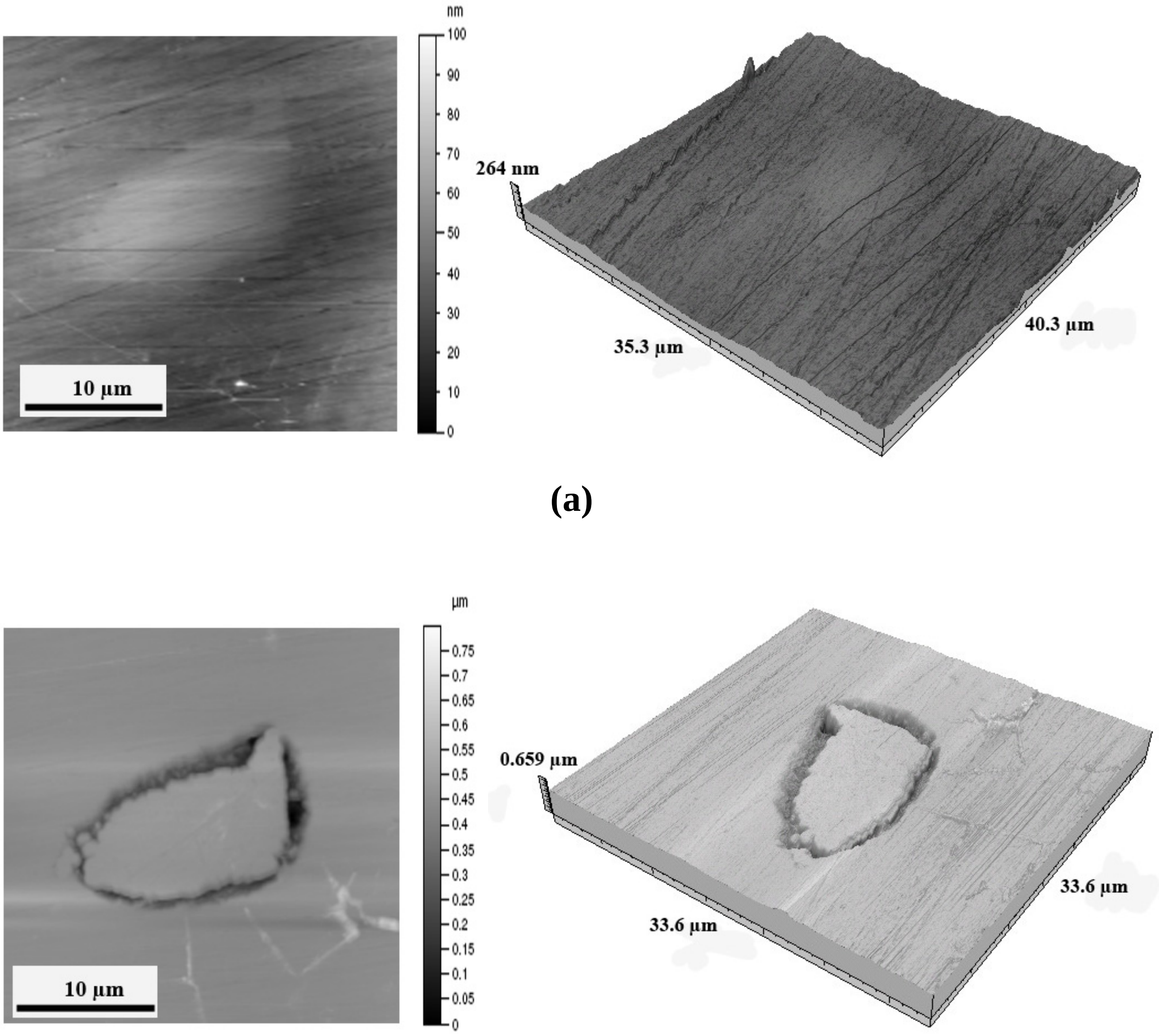

(a)

(b)

Figure 5.27 AFM images of a Fe-Mn particle; (a) before test, (b) after potentiostatically polarizing at a cathodic potential of -1000 mV vs. Ag/AgCl in naturally aerated 0.1 M NaCl for 10 minutes using a capillary of 40 µm diameter. Current density as a function of time during the potentiostatic polarization of the Fe-Mn particle is shown by the black curve in Figure 5.25.

An initial sharp increase in the current found for ‘S’ phase particle (Figure 5.28) is probably due to the selective dissolution of Mg from the particle. Once the Mg (and Al) starts dissolving selectively, the surface becomes enriched with copper, which is an active place for oxygen reduction. As a result, the net current is negative (Figure 5.28). These observations from the potentiostatic tests on ‘S’ phase particles support the observations from the potentiodynamic scans as seen from Figure 5.23. In both cases rapid increase in the current density is followed by the decrease in the current density consistent with the selective dissolution of Mg from the ‘S’ phase particles. When an area containing mixed phase (‘S’ phase + Fe-Mn) particle was exposed, the decrease in current seems to be less sharp compared with the ‘S’ phase particle (Figure 5.29). No change in the current is observed for Fe-Mn particle, and it remained cathodic.

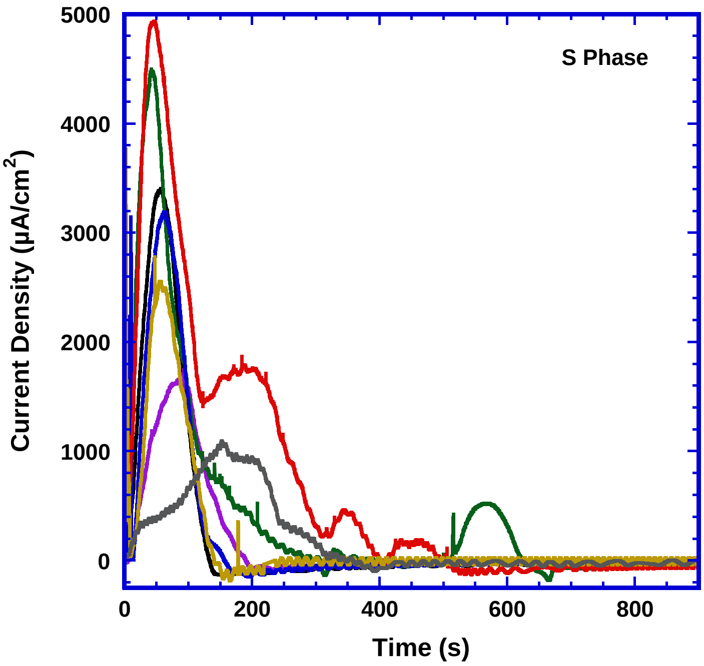

Figure 5.28 Potentiostatic measurements on ‘S’ phase particles at E = -600 mV vs. Ag/AgCl in naturally aerated 0.1 M NaCl using a capillary of 40 μm diameter. Initial rapid increase in the current is possibly due to the dissolution of Mg from the ‘S’ phase particles.

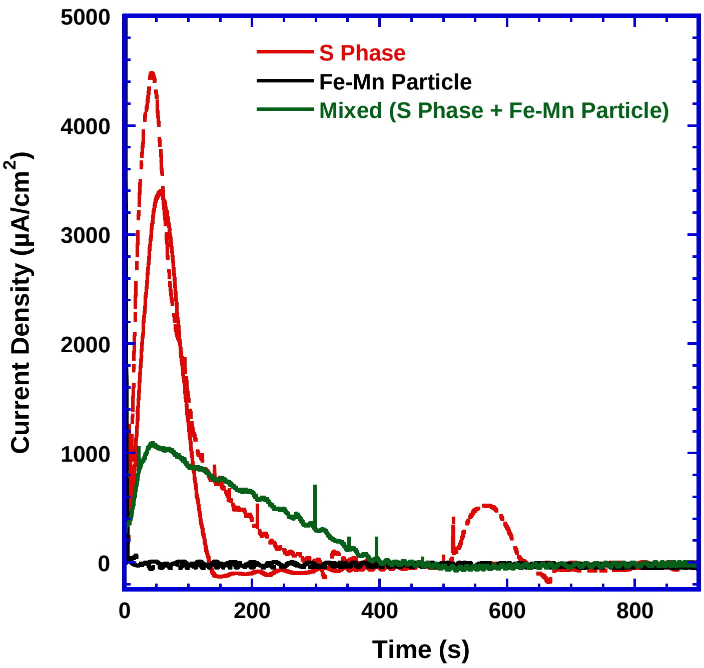

Figure 5.29 Potentiostatic measurements on different particles of AA2024-T351 at E = -600 mV vs. Ag/AgCl in aerated 0.1 M NaCl using a capillary of 40 µm diameter. Higher current associated with the 'S' phase particles confirm their active nature over the Fe-Mn particles.

Figure 5.30 and Figure 5.31 show the SEM micrographs of the 'S' phase particles and Fe-Mn particles, respectively, before and after the potentiostatic test at -600 mV vs. Ag/AgCl for 15 minutes (potentiostatic curves for the respective particles can be found in Figure 5.29). 'S' phase particle seems to be attacked at/around the edges (Figure 5.30) whereas the Fe-Mn particle (Figure 5.31) does not show any significant change in the morphology even after the test.

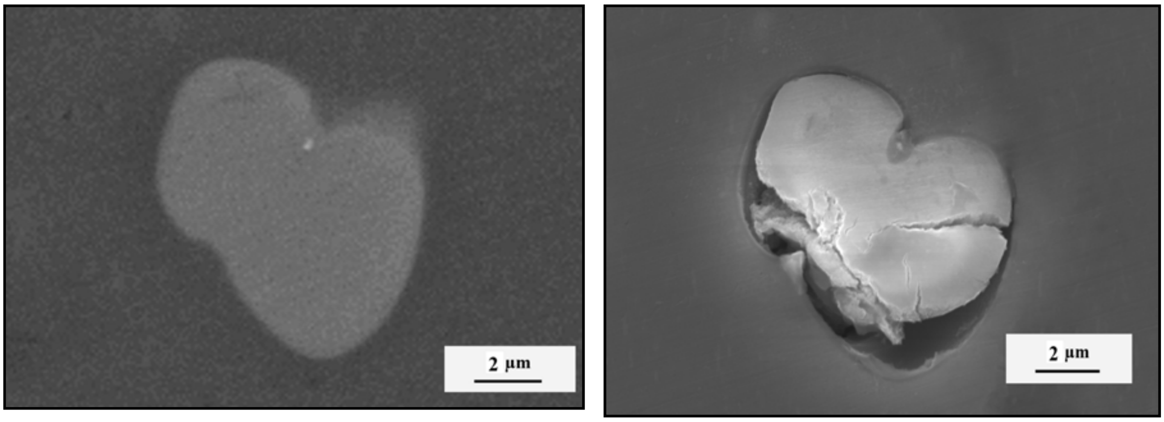

(a) **(b)**

Figure 5.30 SEM images of ‘S’ phase particle (a) before and (b) after the potentiostatic test (represented by the firm red line in Figure 5.29) at E = -600 mV vs. Ag/AgCl (particle is anodic) in aerated 0.1 M NaCl for 15 mins. Attack and dissolution of the ‘S’ phase particle is clearly visible.

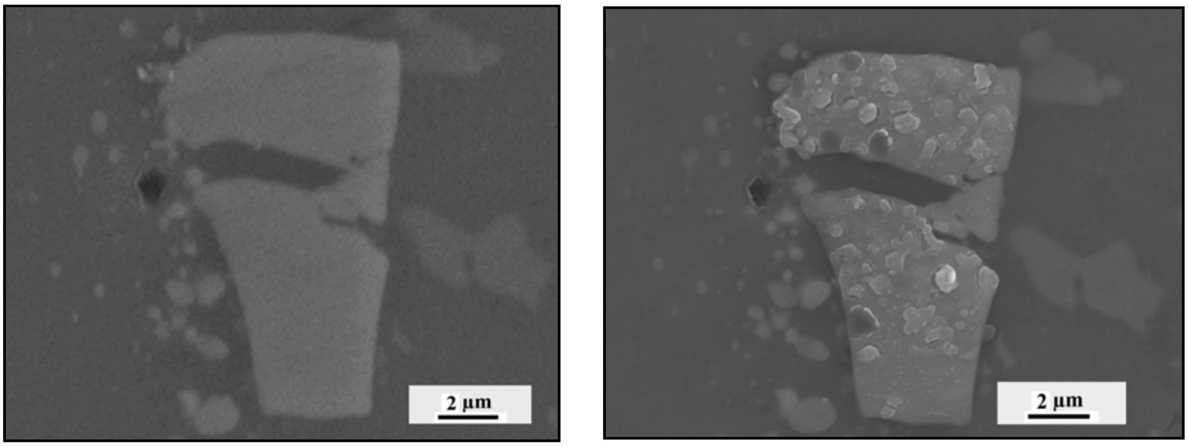

(a) **(b)**

Figure 5.31 SEM images of a Fe-Mn particle (a) before and (b) after the potentiostatic test (represented by the black curve in Figure 5.29) at E = -600 mV vs. Ag/AgCl (particle is cathodic) in naturally aerated 0.1 M NaCl for 15 mins (40 µm diameter capillary). No apparent changes in the particle morphology are observed due to the exposure.

A number of ‘S’ phase particles were subjected to EDS analysis before and after the test to confirm any changes in the composition of the particles. Figure 5.32a-b represents the composition linescans on the ‘S’ phase (shown in Figure 5.30) before and after the potentiostatic test. Before the exposure, magnesium and copper are homogeneously distributed across the ‘S’ phase particle whereas after the test the surface is clearly enriched with copper. The oxygen observed after the test is likely to come from the corrosion product.

Figure 5.33a-b show the EDS spectrum and the elemental analysis of a number of ‘S’ phase particles before and after potentiostatic tests at -600 mV vs. Ag/AgCl in naturally aerated 0.1 M NaCl. Selective dissolution of Mg and Al from the ‘S’ phase particle is confirmed by EDS elemental analysis, where Mg dissolution is the most severe. This is consistent with previous observations by other researchers [182, 211]. A typical ‘S’ phase particle contains ~40-45 wt% Al, 40-46 wt% Cu, and 15-18 wt% Mg. After the potentiostatic tests, copper content of the particle surface increased as high as 80 wt%, whereas aluminium content decreased to ~15-20 wt%. Mg dissolution is most severe and after potentiostatic tests ‘S’ phase particles contain very little Mg, Figure 5.33b.

Figure 5.34a-b shows the EDS spectrum and the elemental analysis, respectively, of Fe-Mn particles before and after the potentiostatic test. Fe-Mn particles do not show any significant difference in the composition before and after the tests. Moreover SEM analysis of the particles after the test does not reveal any attack on the Fe-Mn particles or around the particles (at -600 mV vs. Ag/AgCl) [e.g., Figure 5.31].

Figure 5.35 shows the morphology of an ‘S’ phase particle before the potentiostatic test (at -600 mV vs. Ag/AgCl) and after partial exposure during the test. The capillary is placed in such a way that position (1) and (2) on the particle is fully exposed whereas position (3) and (4) is partially exposed as they remain under the silicone rubber coating on the glass tip. Some attack can be seen in the fully exposed part [next to position (1)], whereas partially exposed part do not show any significant changes.

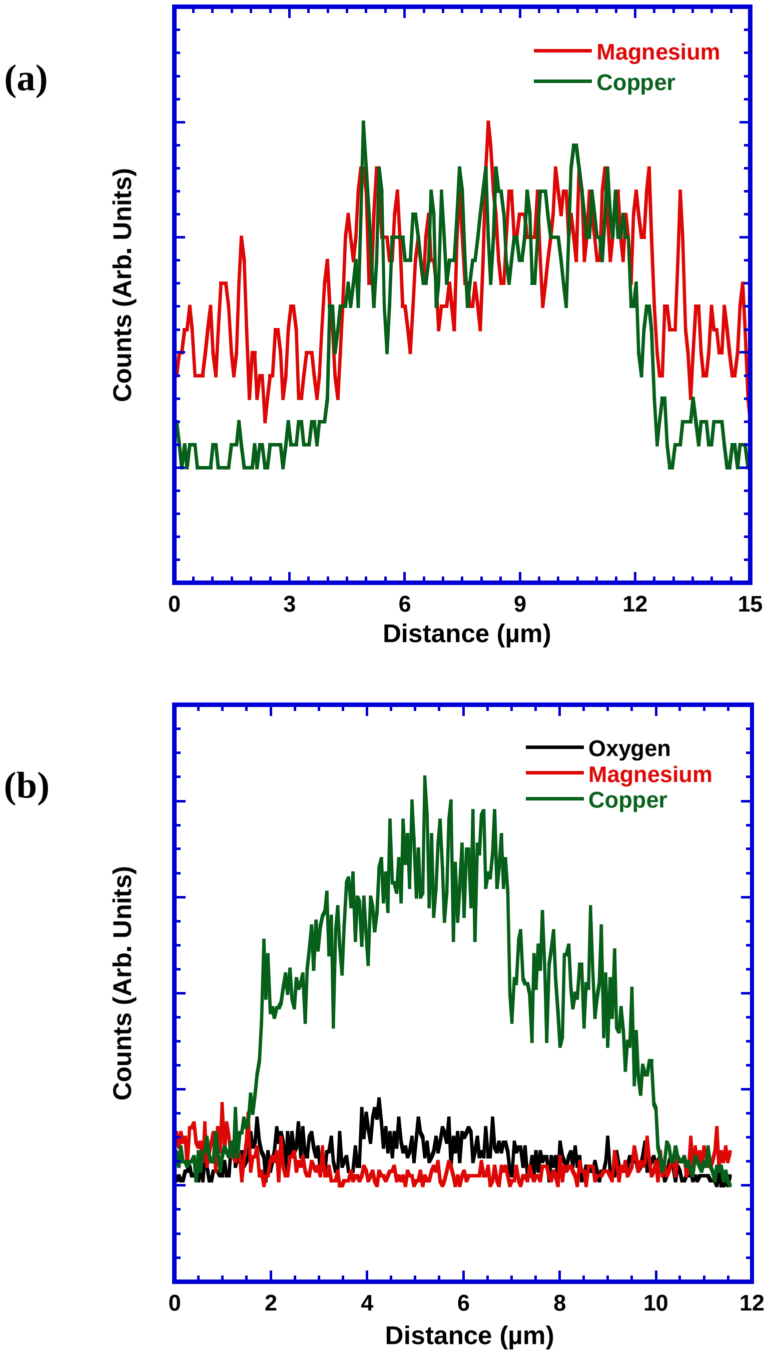

Figure 5.32 EDS linescans across the ‘S’ phase particle (shown in Figure 5.30), (a) before test and (b) after the potentiostatic test at E = -600 mV vs. Ag/AgCl (particle is anodic) in naturally aerated 0.1 M NaCl for 15 mins (40 μm diameter capillary). Copper enrichment on the surface of the ‘S’ phase particle can be seen after the potentiostatic tests.

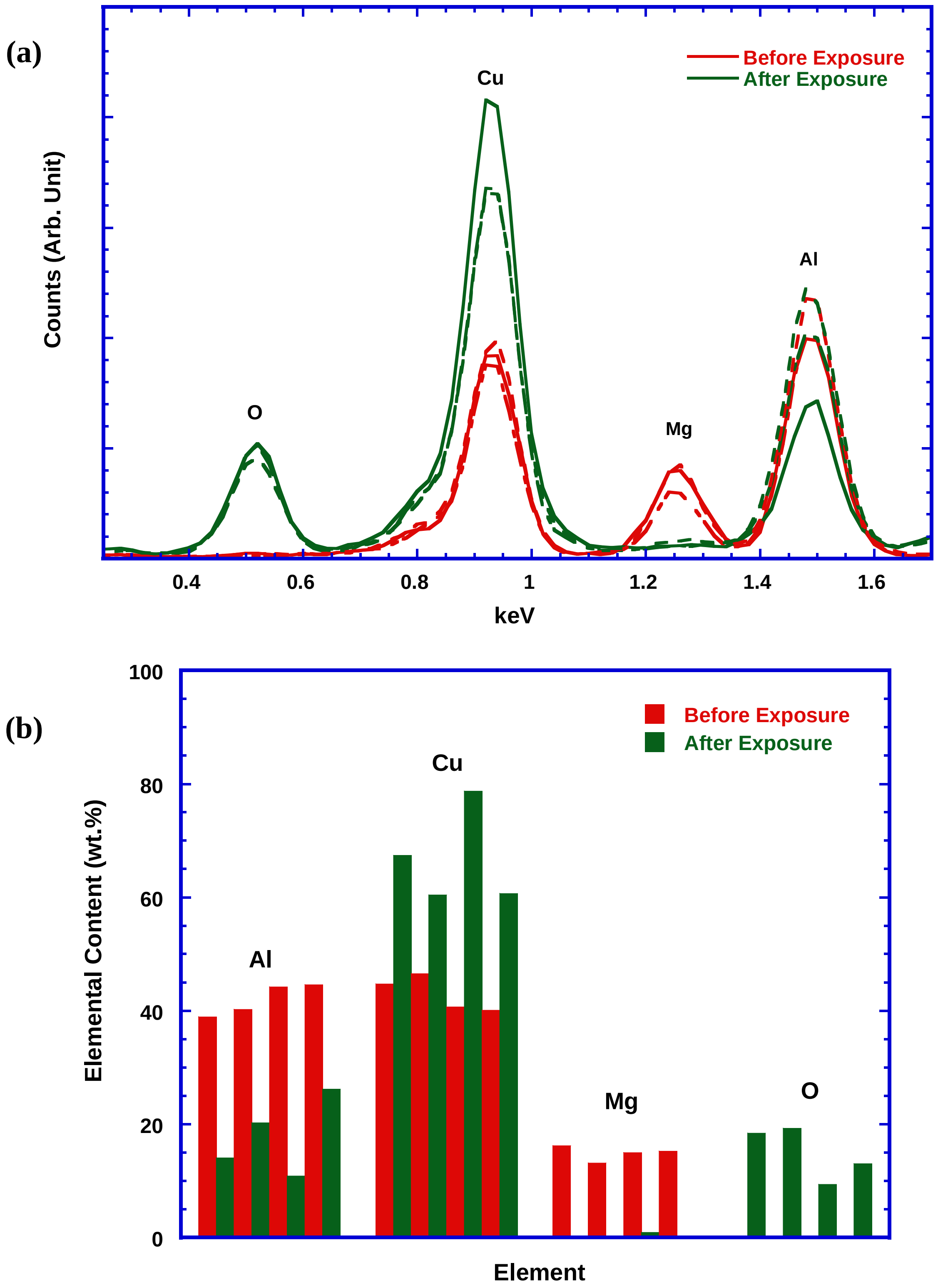

Figure 5.33 Comparison of (a) EDS spectrums from the centre of 'S' phase particles, and (b) elemental composition of the 'S' phase particles, before and after the potentiostatic test at E = -600 mV vs. Ag/AgCl (particle is anodic) in naturally aerated 0.1 M NaCl for 15 mins (40 µm diameter capillary). Mg dissolution and Cu enrichment on the 'S' phase particles can be seen from the analysis.

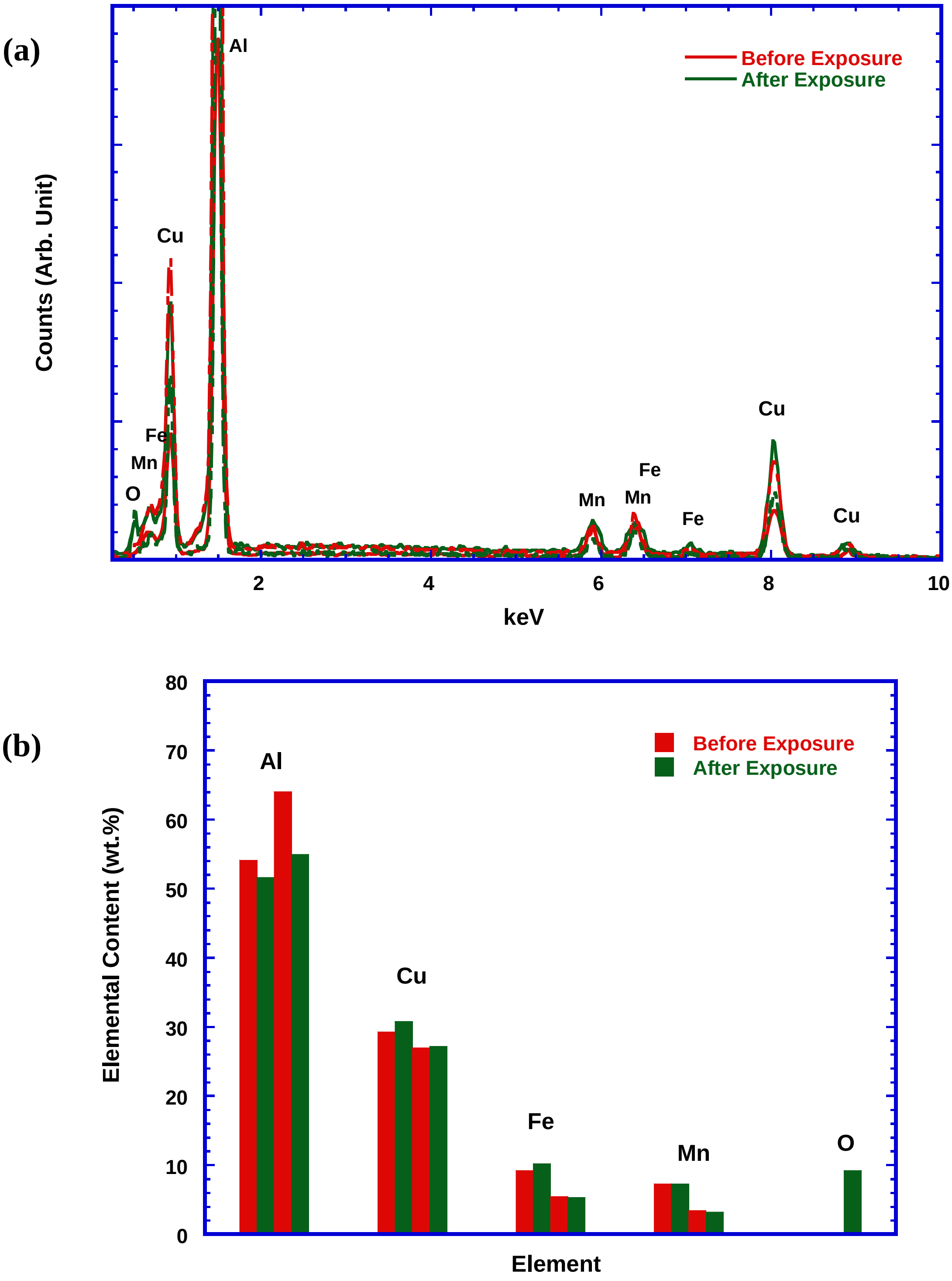

Figure 5.34 Comparison of (a) EDS spectrums from the centre of Fe-Mn particles, and (b) elemental composition of the Fe-Mn particles, before and after the potentiostatic test at E = -600 mV vs. Ag/AgCl (particle is cathodic) in naturally aerated 0.1 M NaCl for 15 mins (40 µm diameter capillary).

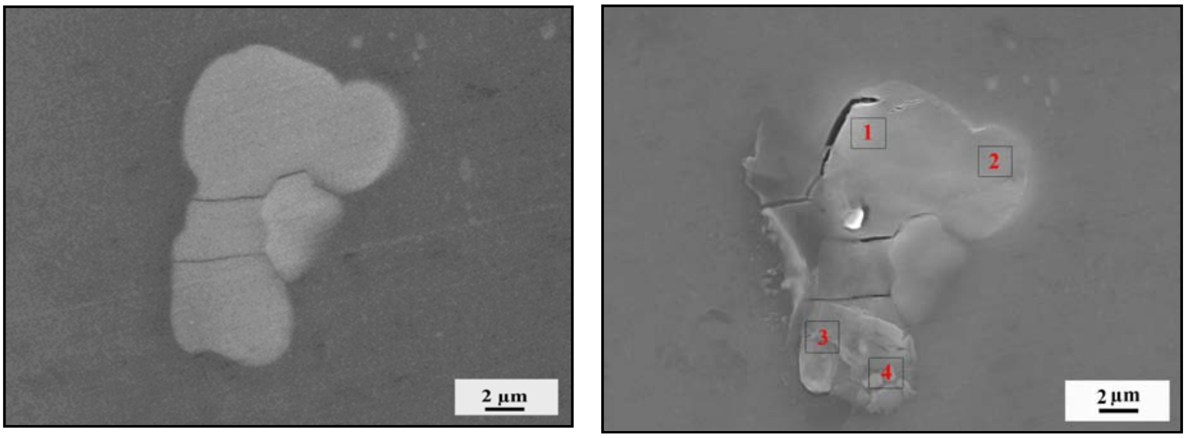

(a) **(b)**

Figure 5.35 SEM images of a partially exposed ‘S’ phase particle (a) before and (b) after the potentiostatic test at E = -600 mV vs. Ag/AgCl (particle is anodic) in naturally aerated 0.1 M NaCl for 15 mins (40 µm diameter capillary). Positions 1 and 2 are fully exposed while positions 3 and 4 are partially exposed.

Figure 5.36 shows the EDS spectrum and the elemental analysis of ‘S’ phase particle [shown in Figure 5.35] before and after partial exposure during the potentiostatic test. Mg dissolution happened extensively in the fully exposed portion [e.g. position (1)]. Partial exposure does not enrich the surface with copper (rather it shows slightly less copper), and some amount of Mg still remains in the partially exposed positions of that ‘S’ phase particle. The unexposed part of the particle remains at the same composition as the initial particle.

Figure 5.37 shows the morphology of an ‘S’ phase particle and a Fe-Mn particle before and after the potentiostatic test (at -600 mV vs. Ag/AgCl) when they are exposed together. Attacks have been found on/around the ‘S’ phase particles only with no apparent change in the Fe-Mn particle morphology. This observation firmly confirms that the reactivity of ‘S’ phase particles is higher than the Fe-Mn particles. Figure 5.38 shows the elemental analysis before and after the potentiostatic test (at -600 mV vs. Ag/AgCl) when both ‘S’ phase particle and Fe-Mn particle are exposed together (as in case of Figure

5.37). Fe-Mn particle do not show any compositional change whereas ‘S’ phase particles shows Mg dissolution and copper enrichment after the exposure.

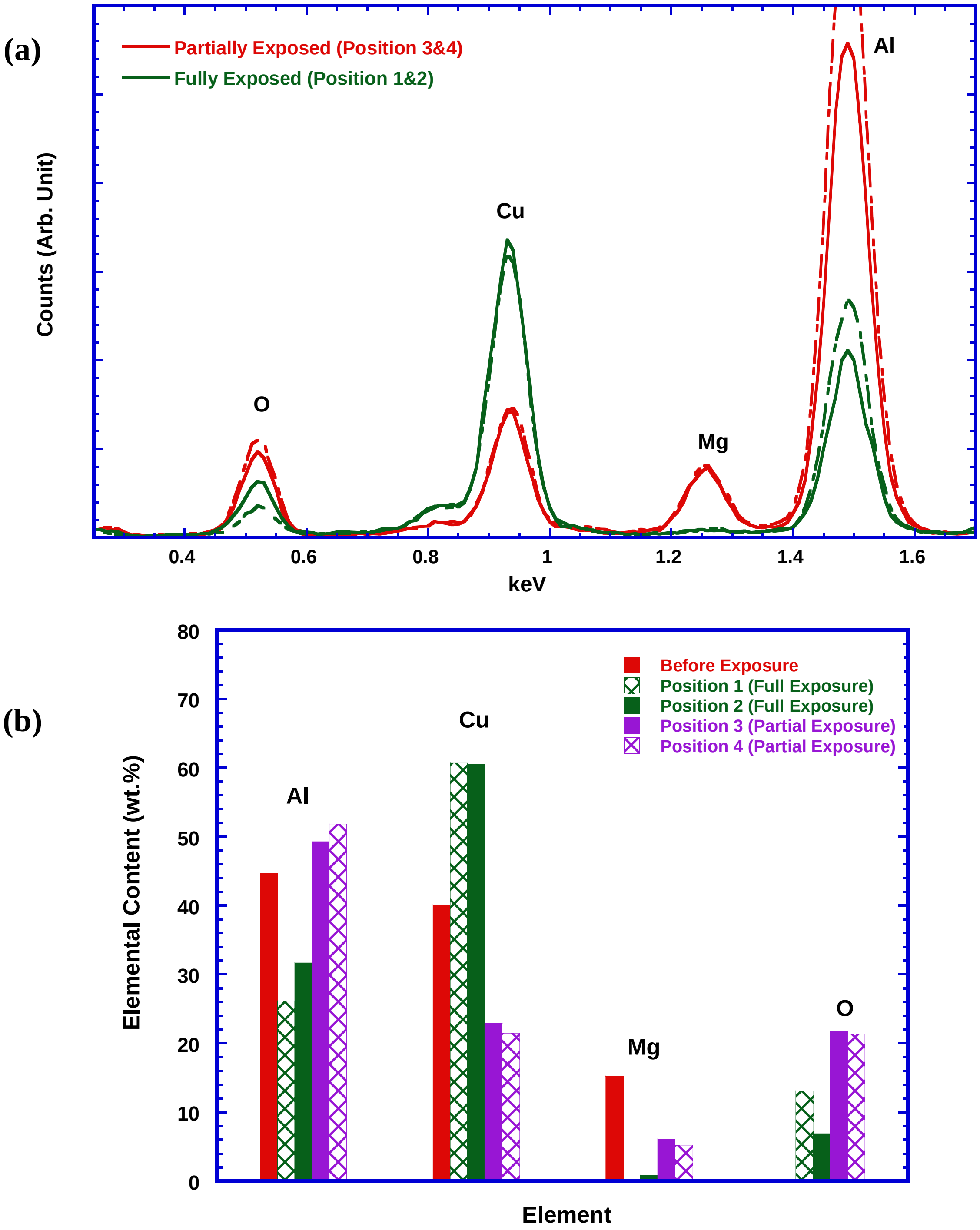

Figure 5.36 Before and after exposure comparison of, (a) EDS spectrums and (b) Elemental composition, from the partially exposed ‘S’ phase particle potentiostatically tested at E = -600 mV vs. Ag/AgCl (particle is anodic) in naturally aerated 0.1 M NaCl for 15 mins (40 μm diameter capillary).

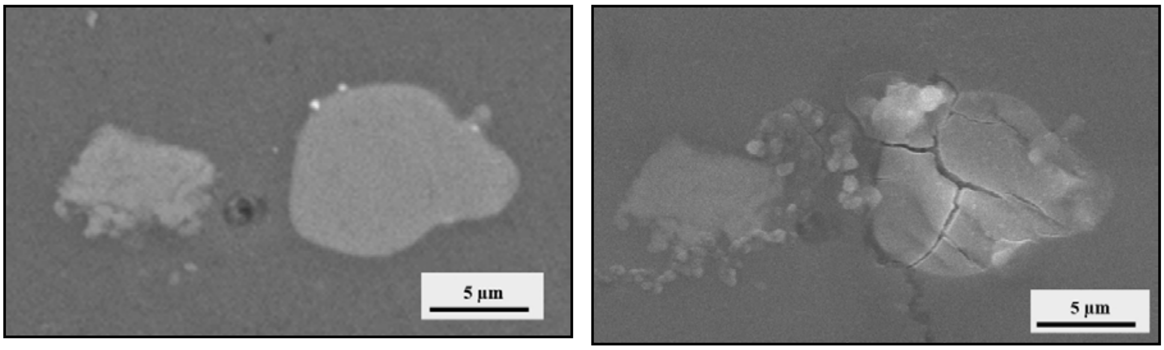

(a) **(b)**

Figure 5.37 (a) Before and (b) after exposure SEM images of ‘S’ phase particle and Fe-Mn particle when both were potentiostatically tested together at E = -600 mV vs. Ag/AgCl in naturally aerated 0.1 M NaCl for 15 min (40 µm diameter capillary). At this polarization potential, ‘S’ phase particle is active whereas Fe-Mn particles behave cathodically.

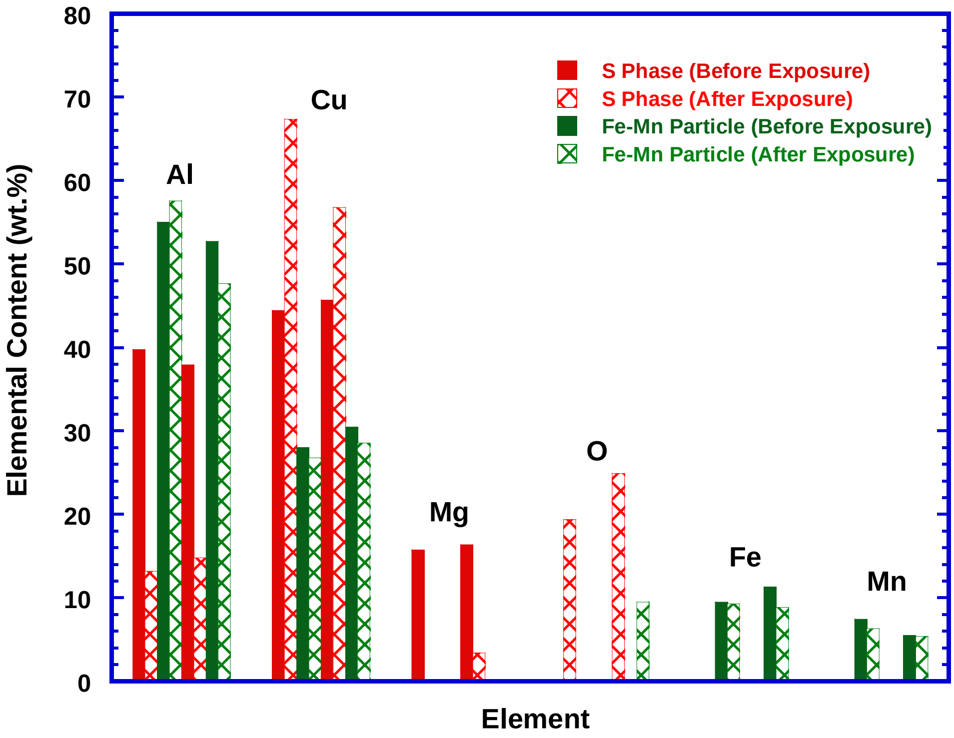

Figure 5.38 Before and after exposure elemental analysis of ‘S’ phase particle and Fe-Mn particle when both were potentiostatically tested together at E = -600 mV vs. Ag/AgCl in naturally aerated 0.1 M NaCl for 15 min (40 µm diameter capillary). At this holding potential, ‘S’ phase particle is active whereas Fe-Mn particles behave cathodically.

5.3 Discussion

Two categories of intermetallic particles have been classified on the surface of aluminium alloy 2024. The first type appeared as round and smooth with size range of 1-5 µm and identified as Al_2CuMg (‘S’ phase). The second type of particle (consists of Al-Cu-Fe-Mn) is in the range of 10-20 µm with rectangular or elongated shape and identified with the composition of $Al_6(Cu,Fe,Mn)$ or other stoichiometric relationship [‘Fe-Mn’ particle] [9, 11].

As described earlier, pitting in aluminium alloys is normally associated with these types of intermetallic/constituent particles. The role of these intermetallic particles in initiating localized corrosion has been investigated by different researchers in last few decades using several electrochemical and characterization techniques [7-9, 11, 14, 19, 37, 38, 40-48, 82, 123, 171, 173-175, 181-200]. However, the exact mechanisms behind the pit initiation are still a subject of debate and many alternative theories[19] have been proposed to explain the observed corrosion phenomena.

In most of the cases, experiments are performed on the bulk aluminium alloy itself and the morphology of the intermetallic particles are characterized during the exposure and after the exposure. Though these techniques capture the real behaviour of the alloy, the exposure of the bulk material makes it difficult to separate the contribution from different intermetallic phases towards corrosion. So, bulk alloys have been synthesized to simulate the composition of the Fe-Mn particle and the ‘S’ phase particles. The corrosion potentials of these intermetallic particles have been measured to have a better understanding of the importance of the intermetallic particles as initiation sites for

---

[19] See Section 2.2.1.3.1 of Chapter 2 for more details.

corrosion [201, 202]. Corrosion potentials of different phases present in AA2024-T3 have been compiled by Buchheit [14, 191] and others [18] [summarized in Table 2.2 in Chapter 2]. These measurements on bulk intermetallic samples indicate the relative nobility of the two main types of particles in AA2024-T3; Fe-Mn particles should be more noble relative to the Al matrix, whereas 'S' phase particles should be more active [191, 204].

The micro-capillary electrochemical cell technique gives the opportunity to revisit some the proposed theories for pit initiation as this technique can expose a very small area of interest within the real bulk alloy. In this current study, a capillary diameter of 40 μm has been used to study the behaviour of Fe-Mn particles, 'S' phase particles, and the particles free matrix in AA2024-T351. Effort has also been made to rank those phases according to their relative corrosion susceptibility.

5.3.1 Effect of Cathodic Polarization on the Corrosion Behaviour of Intermetallic Particles

Potentiodynamic scans in this current study (shown in Figure 5.1, Figure 5.2, and Figure 5.3) emphasize the role of prior cathodic polarization in determining the corrosion properties of different phases. The relative corrosion behaviour of different phases (intermetallic particles in particular) is seen to depend of the polarization history (in this case the extent of cathodic polarization during the potentiodynamic scan). However, from the comparison of the corrosion behaviour of different phases (as seen in Figure 5.4 and Figure 5.5), it is quite clear that irrespective of the polarization history, the 'S' phase particle is the most active phase in AA2024-T351 and thereby consistent with the findings of other researchers [8, 12, 37, 43, 46, 174, 185, 198]. ‘S’ phase particles show a lower breakdown potential as well as lower corrosion potential than the matrix of AA2024-T351 as reported by those researchers.

Fe-Mn particles showed higher cathodic reactivity with lowering of the scan start potential (Figure 5.1 and Figure 5.2 vs. Figure 5.3), whereas particle free matrix of AA2024-T351 does not show any significant change in the cathodic reactivity as a function of scan start potential. When the potentiodynamic scans are started from -700 mV vs. Ag/AgCl, the matrix show a higher breakdown potential than the Fe-Mn particles. However, when the scans are started from -1000 mV vs. Ag/AgCl, Fe-Mn particles show higher breakdown potentials as well as higher corrosion potentials than both the matrix and ‘S’ phase particles. These differences in the corrosion behaviour of Fe-Mn phases can probably be attributed to the change in the particle surface or increase in the local alkalinity as a result of their longer duration in the cathodic domain.

Changes in the Fe-Mn particle surface could be confirmed from Figure 5.6 and Figure 5.7. These two figures show that when a scan starts from -1000 mV vs. Ag/AgCl, the Fe-Mn particle surface turns black, whereas scan from -700 mV vs. Ag/AgCl do not change the appearance of the particle. It is generally believed that Fe-Mn particles act as cathodes during the corrosion process as the corrosion potential of Fe-Mn particles is nobler than the matrix [8, 11, 191]. As the predominant cathodic reaction for aluminium corrosion is oxygen reduction, a local increase in the pH will occur on Fe-Mn particles during the potentiodynamic scans.

Under alkaline conditions, aluminium is dissolved from the intermetallic particles, causing the surface to become enriched in Cu (also with Fe and Mn) by dealloying. The enriched Cu (along with Fe and Mn) component depolarizes the cathodic reactions causing a positive shift in the corrosion potential measured during the scan [14]. A longer duration of the cathodic portion increases the chance of local increase in the alkalinity around the Fe-Mn particles. This could be the possible reason for observing black layer on Fe-Mn particles from -1000 mV vs. Ag/AgCl scans and not from -700 mV vs. Ag/AgCl scans. The composition of this black layer is not known yet as EDS analysis on the particles with and without the black layer could not resolve the differences. However, Schmutz and Frankel [43, 44] emphasized the role of such surface layers on the particles (specially on Mg containing phases) as well as on the matrix in determining the corrosion properties of AA2024-T3. They found some ‘S’ phase particles to be nobler than the matrix due to the presence of altered surface films while using Scanning Kelvin Probe Force Microscopy.

5.3.2 Sites of Pit Initiation

As discussed earlier, ‘S’ phase particles are found to be the most active phase in the AA2024-T351. SEM analysis of the ‘S’ phase particles do not reveal any severe attack on them (Figure 5.11) if the potentiodynamic scan (represented by the red curves in Figure 5.1) is stopped right after the initial rapid increase in the current. Hence, the findings in this current study are consistent with observations of other researchers who have confirmed the initial anodic behaviour of ‘S’ phase particles by showing the initiations of pits on the ‘S’ phase particles [8, 12, 37, 43, 46, 174, 185, 198]. However, continuation of a potentiodynamic scan beyond the initial dissolution (due to the selective dissolution of Mg) zone leads to the dissolution and attack on the ‘S’ phase particles (Figure 5.23 and Figure 5.24). These observations are consistent with the findings of Suter and Alkire [40] where they did not find any adsorbed copper around the inclusions when the experiments were stopped during pit initiation (I_{max} : 10 nA), but adsorbed copper was found when the experiments were stopped during pit propagation (I_{max} : 1 μm).

By comparison, observations of the attack morphology on the Fe-Mn particles in this current study can not be explained by a single prevailing/dominant mechanism. Several mechanisms are possibly operating and thereby resulting pitting is observed in the particle (Figure 5.8), pitting at the edge of the particle (Figure 5.9a and Figure 5.10b) and even at the matrix adjacent to the periphery of the particle (Figure 5.8b and Figure 5.10a). There is also no definite correlation between the attack morphology and the scan start potential. As the Fe-Mn intermetallic particles act as cathode during the corrosion process, severe dissolution of these particles is not expected though pitting sometime occurs at their periphery, Figure 5.9a and Figure 5.10b. These observations are consistent with the finding of other studies [7, 8, 11, 175, 186, 187]. In some cases attack on Fe-Mn particles had been observed due to their heterogeneous nature, Figure 5.8a and Figure 5.9b [43, 44]. Interestingly, in a few cases, attack has been observed at the adjacent matrix without any visible change in the Fe-Mn particles, Figure 5.8b and Figure 5.10a. Liao *et al.* [179] suggested that pitting corrosion is induced by the galvanic interaction between the particle-matrix couple, with the particles promoting matrix dissolution. They also concluded that the galvanic coupling is responsible not only for the nucleation but also the growth of pits.

Localized attack on the matrix phase is typically a hemispherical pit showing crystallographic corrosion facets in the internal surfaces (Figure 5.12) or a cluster of small pits showing crystallographic corrosion tunnels in the internal surfaces (Figure 5.13).

5.3.3 Trenching Around the Intermetallic Particles

Localized corrosion of aluminium alloys associated with the intermetallic particles is explained by several researchers using a cathodic trenching phenomena which was originally introduced by Nisancioglu *et al.* [208]. These type of trenching formation between the matrix and the intermetallic particle has been extensively discussed in the literature [8, 40, 43, 48, 171, 175, 186, 198, 209]. A few authors [48] argued that these grooves/cavities may switch to an acid-pitting mechanism at later stages, whereas other researchers refer to the alkaline attack itself as pitting [11, 170] or described the grooving phenomena as galvanic corrosion between particle and matrix [9]. The cathodic trenching model (as proposed by Nisancioglu) deals with the local increase in the pH adjacent to the cathodic particles as a result of the oxygen reduction reaction on them. At higher pH the passive film on aluminium dissolves and thereby enhances the matrix dissolution.

Several sets of experiments were performed in this present study to investigate the nature of the trenching/grooving around the intermetallic particles. Efforts have also been made to gain a better understanding about the possible mechanism (alkaline vs. acidic) of trench/groove formation.

It is evident in this study that the formation of these trenches is not necessarily related to the pitting phenomena as they appear in the scans which were stopped before reaching the pitting potential (Figure 5.15 and Figure 5.22). Through a series of potentiodynamic experiments (Figure 5.17) from different scan start potentials it is shown that the grooving around the Fe-Mn particles is most probably caused by the local increase in the alkalinity. Grooving was always observed when the scan is started from -1000 mV vs. Ag/AgCl (thereby having longer time in the cathodic domain) as opposed to the scans started from -700 mV vs. Ag/AgCl (shorter time in the cathodic domain) showing pitting attack at the particle/matrix interface (Figure 5.18 and Figure 5.19 vs. Figure 5.20).

Presence of very tight micro or nano crevices at the particle/matrix interfaces could play an important role in initiating localized corrosion (will be discussed in Chapter 6 in detail). Longer duration of the cathodic polarization will generate more alkalinity which may create alkaline grooving around the particles. These relatively wider grooves can alter the geometry of tight crevices and thereby minimize the chance of initiating pits. This increase in local alkalinity may also make the transition from metastable to stable pitting difficult (see Chapter 4 for more details about the role of local alkalinity on the metastable pitting). Thus the alkaline trenching model can be used to explain the higher breakdown potential of the Fe-Mn particles as seen from the potentiodynamic scans from -1000 mV vs. Ag/AgCl which shows grooving around the particle as opposed to scans from -700 mV vs. Ag/AgCl which does not necessarily show grooving. However it should also be remembered that irrespective of pit initiation sites, increase in local alkalinity makes pit initiation difficult. So, increase in the solution pH inside the micro-capillary can also play a role in increasing the breakdown potential of the Fe-Mn particles during the potentiodynamic scans from -1000 mV vs. Ag/AgCl.

It is interesting to note that some Fe-Mn particles show discontinuous grooving around them (Figure 5.18 and Figure 5.19) where other Fe-Mn particles show continuous grooving (Figure 5.22) though all of them were started from -1000 mV vs. Ag/AgCl. These observations could be correlated with the findings of Rynders *et al.* [47] who used in situ AFM to study the trench formation near iron rich inclusions (as shown in Figure 2.12 in Section 2.2.1.3 of Chapter 2). Initial trenching around the particles was non uniform in some cases and normally observed in the regions where the ratio of inclusion: host matrix surface area was high [47]. However, at the later stages of the trench formation around the particle, dissolution of the surrounding matrix became uniform and proceeded radially outward from the inclusion edge. Rynders *et al.* [47] attributed the shape evolution of the initial non uniform trenches around the particles to the size and shape of the inclusions, local accumulation of hydroxide, and rate of transport of oxygen.

As described earlier, in the alkaline model the main reason for cathodic trenching is thought to be the increase in the local pH. However, Schneider *et al.* [38] argued that this ‘alkaline’ model is not efficient enough to rationalize trenching at low pH and also could not properly explain different trenching phenomena associated with different types of particles. So, an alternate anodic trenching model based on the assumption of galvanic coupling between the matrix and the particles causing preferential breakdown or enhanced passive dissolution was proposed. Formation of copper rich intermetallics leads to the depletion of Cu in the adjacent matrix [7, 9, 173, 194]. A lower Cu content in the matrix lowers the pitting potential and promotes pitting at specific locations [37, 210]. It is possible that pitting attack (Figure 5.20) at the edge of the Fe-Mn particle is initiated due to this type of galvanic coupling.

Terminating potentiodynamic scans (Figure 5.21) before reaching the corrosion potential, just before the pitting potential and after the pitting potential do not change the appearance of the grooving around the Fe-Mn particle (Figure 5.22). These observations using AFM are consistent with the earlier findings using optical profilometer (Figure 5.15 and Figure 5.16) in higher concentration (0.5 M NaCl) of sodium chloride solution. It is worth noting that optical profilometry on the Fe-Mn particle after the polarization scan in 0.5 M NaCl always show continuous and wider grooving around the particle as opposed to the narrower continuous or discontinuous grooving (revealed through AFM analysis) after polarization scan in 0.1 M NaCl. This possibly emphasizes the role of solution concentration on the corrosion behaviour of the particle as well. However, consistency of the grooving around the Fe-Mn particles irrespective of their pitting/breakdown phenomena confirms the alkaline origin of these grooving.

The presence of alkaline grooving around Fe-Mn particles and ‘S’ phase particles was confirmed with further potentiostatic polarization tests at a cathodic potential (-1000 mV vs. Ag/AgCl). ‘S’ phase particles are more cathodically active than the Fe-Mn particles as indicated by the higher cathodic current of ‘S’ phase particles during the potentiostatic tests, Figure 5.25. This is consistent with the findings of Kolics *et al.* [215] and Aldykiewicz *et al.* [216] who used a Ce decoration technique to detect cathodically active sites. Sites with higher Ce deposition indicate the higher the cathodic reactivity of that site. Kolics *et al.* [215] found the highest Ce deposition on the ‘S’ phase particles followed by Fe-containing particle and matrix.

An increase in the local alkalinity due to the oxygen reduction can lead to the dissolution of Al from the particles and thereby enriching the particle surface with copper. As copper provides a better surface for oxygen reduction, cathodic current increases gradually during the initial stage of potentiostatic tests (Figure 5.25). However, the current densities become stable after almost 10 minutes at a cathodic polarization. ‘S’ phase particles show deep alkaline grooving around them as shown in Figure 5.26. However in a few cases grooving around the ‘S’ phase particles was not very deep and was spread over the adjacent matrix. These differences in the behaviour of ‘S’ phase particles could be explained by the inert nature of some ‘S’ phase particles or due to the differences in the reactivity of different ‘S’ phase particles. Differences in the behaviour of ‘S’ phase particles have also been reported in the work of other researchers [12, 43, 44]. Using the microreference electrode technique Shao *et al.* [12] found that some ‘S’ phase particles are non-reacting with no attack around the periphery. It was assumed that these particles must have been protected by some kind of film that dissolves very slowly in NaCl solution [43]. Schmutz *et al.* [43, 44] found the presence of surface film on ‘S’ phase particles when they used ex situ AFM topographic and Volta potential mapping (Kelvin Probe Technique) to examine the corrosion that occurred at different intermetallics particles in AA2024-T3 during immersion in NaCl solution. Differences in grooving extent and appearances have also been observed around the Fe-Mn particles. These could also be attributed to the local inhomogeneities in the Fe-Mn particles as described in other work [43, 44].

Further examples of grooving around ‘S’ phase particles can be seen in Figure 5.30. These grooving occurred during the potentiostatic polarization of the ‘S’ phase particles in the anodic domain (see Figure 5.28). Grooving around ‘S’ phases particles may occur due to the local increase in the alkalinity (enhanced oxygen reduction reaction at the copper enriched particle) and therefore alkaline corrosion of surrounding aluminium matrix. This kind of grooving around the ‘S’ phase particles has been reported recently by Zhu [211]. Zhu [211] suggested that the dissolution around the ‘S’ phase particles takes place as a result of alkaline corrosion rather than galvanic coupling as suggested by Buchheit [9] and a few other researchers [7]. In another recent study on the modelling of corrosion of synthetic ‘S’ phases, Blanc *et al.* [317] agreed with the phenomenon of alkaline grooving around the ‘S’ phase particles. The findings in this current study are consistent with Liu *et al.* [29] who found trenching around ‘S’ phase particles and depletion of Mg from ‘S’ phase particles after potentiostatic polarization at -660 mV vs. SCE in deaerated 1M NaCl for 1h.

5.3.4 Dissolution Characteristics of the 'S' Phase Particles

Potentiostatic tests on the 'S' phase particles in the anodic domain (at -600 mV vs. Ag/AgCl as shown in Figure 5.28) show the appearance of grooving around the 'S' phase particles as well as attack on them (Figure 5.30). The initial rapid increase in the current density during the potentiostatic test is due to the Mg dissolution. Selective dissolution of Mg and Al from the 'S' phase particles has been proved by EDS elemental analysis (Figure 5.33), where Mg dissolution is the most severe. Once Mg (and Al) is selectively dissolved from the 'S' phase particles, the surface becomes enriched with copper (Figure 5.32 reveals the EDS line scans showing the copper enrichment on the surface of 'S' phase particles after exposure) which is better place for oxygen reduction. As a result the net current tends to be negative as seen by the gradual decrease in the i-t curve (Figure 5.28). Hence the assumption of several researchers [8, 173, 175, 182, 186] including the experimental evidence shown by others [12, 174, 198, 211] about the selective dissolution of Mg and copper enrichment is confirmed here.

Though the 'S' phase particles show significant change in composition at this particular polarization potential (i.e., -600 mV vs. Ag/AgCl), no significant difference in the composition of Fe-Mn particles has been observed before and after similar tests, Figure 5.34. Moreover SEM analysis of the particles after the test does not reveal any attack on the Fe-Mn particles or around the particles (at -600 mV vs. Ag/AgCl). However in Figure 5.31b, some nodular particles are identified which could be pure Cu [211]. Chen *et al.* [8] stated that the Al-Cu-Mn-Fe containing particles function as cathodic sites, which favours cupric ions (Cu^{2+}) dissolved in the NaCl solution to be reduced as nodular Cu deposits on the particles. Obispo *et al.* [80] proved the presence of large deposit of Cu on Fe-rich or Fe-containing areas when AA2024-T3 was immersed in NaCl solution using a TEM/EDX replica technique. They suggested that the reduction of copper from solution is an electrochemical displacement reaction which is very likely to occur on cathodic particles by oxidation or dealloying of electroactive elements such iron out of the particles. At the same time, as the Fe-Mn particles are more cathodic towards the matrix galvanic coupling should be developed between them and thereby induces dissolution of the surrounding Al matrix.

5.3.5 Summary

The findings in this current study (as discussed in the above sections) are consistent with other reported work in terms of the active nature of the ‘S’ phase particles and the existence of grooving around both the Fe-Mn particles and ‘S’ phase particles. It is established that initially ‘S’ phase remain very active and after the selective dissolution of Mg and Al surface of the ‘S’ phase gets enriched with copper. Copper enriched ‘S’ phase particles then favours cathodic reaction which is oxygen reduction in this case and thereby promotes alkaline dissolution around the matrix. By comparison, alkaline grooving around the Fe-Mn particles is clearly seen during the hold at cathodic overpotential. However, the existence of pitting at the particle/matrix interface (in the absence of prolonged cathodic portion) indicates the possibilities of galvanic coupling between the Fe-Mn particle, copper depleted areas around the particle and the matrix. Moreover, this study emphasizes the role of cathodic polarization in determining the corrosion properties of the Fe-Mn particles during the potentiodynamic scans. Surface of the particles could be modified during the cathodic polarization and thereby change the corrosion behaviour of the actual particles. This not only can give wide scatter in the data but it also can give rise to misleading conclusions if careful consideration is not given during the analysis.

5.4 Conclusions

1. Potentiodynamic and potentiostatic polarization scans prove that the ‘S’ phase particles are more active compared to the Fe-Mn particles or the particle free matrix of AA2024-T351.
2. The starting potential (in the cathodic domain) for potentiodynamic scans affected the corrosion behaviour of Fe-Mn particle. This signifies the importance of prior cathodic polarization in the corrosion of aluminium alloys.
3. Pitting has been observed on the Fe-Mn particle, at the edge of the Fe-Mn particle and at the adjacent matrix of the Fe-Mn particle. There is no definite correlation between the location of attack and the scan start potential. Observations of the attack morphology on the Fe-Mn particles in this current study can not be explained by a single prevailing/dominant mechanism. Several mechanisms are possibly operating and thereby resulting pitting in the particle, pitting at the edge of the particle and even at the adjacent matrix.
4. Attack on the ‘S’ phase particles as well as the dissolution around the ‘S’ phase particles have been observed after the potentiostatic and potentiodynamic tests.
5. Optical profilometry and AFM showed presence of grooves around the Fe-Mn particles when scanned from -1000 mV vs. Ag/AgCl (with longer time in the cathodic domain). Scan started from -700 mV vs. Ag/AgCl (shorter time in cathodic domain) show pitting attack at the particle-matrix interface.

6. Presence of continuous and discontinuous alkaline grooving has been seen around the Fe-Mn particles. Oxygen reduction reaction on these cathodic particles increases the local pH which dissolves the passive film of the adjacent alloy matrix and thereby promotes matrix dissolution.
7. The initial sharp increase in the current during the anodic potentiostatic polarization of ‘S’ phase particles is due to the selective dissolution of Mg from the particle. Mg dissolution and Cu enrichment on the ‘S’ phase particles have been confirmed using EDS analysis. Copper enrichment on the surface of ‘S’ phase particles leads to the alkaline grooving around the particles.